JOURNAL OF THE AMERICAN CHEMICAL SOCIETY

Article

pubs.acs.org/JACS

Probing Cation and Vacancy Ordering in the Dry and Hydrated Yttrium-Substituted $BaSnO_3$ Perovskite by NMR Spectroscopy and First Principles Calculations: Implications for Proton Mobility

Lucienne Buannic,[†] Frédéric Blanc,[†,‡] Derek S. Middlemiss,[‡] and Clare P. Grey*[,†,‡]

[†]Department of Chemistry, Stony Brook University, Stony Brook, New York 11790-3400, United States

[‡]Department of Chemistry, University of Cambridge, Lensfield Road, Cambridge CB2 1EW, United Kingdom

Supporting Information

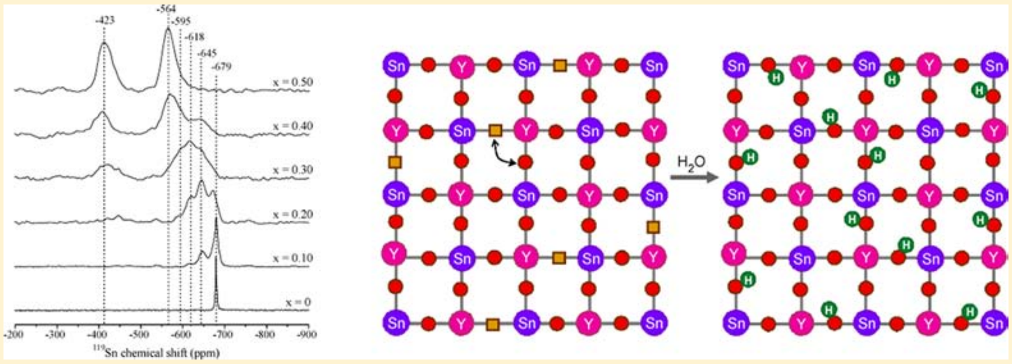

ABSTRACT: Hydrated $BaSn_{1-x}Y_xO_{3-x/2}$ is a protonic conductor that, unlike many other related perovskites, shows high conductivity even at high substitution levels. A joint multinuclear NMR spectroscopy and density functional theory (total energy and GIPAW NMR calculations) investigation of $BaSn_{1-x}Y_xO_{3-x/2}$ ($0.10 \leq x \leq 0.50$) was performed to investigate cation ordering and the location of the oxygen vacancies in the dry material. The DFT energetics show that Y doping on the Sn site is favored over doping on the Ba site. The ^{119}Sn chemical shifts are sensitive to the number of neighboring Sn and Y cations, an experimental observation that is supported by the GIPAW calculations and that allows clustering to be monitored: Y substitution on the Sn sublattice is close to random up to $x = 0.20$, while at higher substitution levels, Y−O−Y linkages are avoided, leading, at $x = 0.50$, to strict Y−O−Sn alternation of B-site cations. These results are confirmed by the absence of a "Y−O−Y" ^{17}O resonance and supported by the ^{17}O NMR shift calculations. Although resonances due to six-coordinate Y cations were observed by ^{89}Y NMR, the agreement between the experimental and calculated shifts was poor. Five-coordinate Sn and Y sites (i.e., sites next to the vacancy) were observed by ^{119}Sn and ^{89}Y NMR, respectively, these sites disappearing on hydration. More five-coordinated Sn than five-coordinated Y sites are seen, even at $x = 0.50$, which is ascribed to the presence of residual Sn−O−Sn defects in the cation-ordered material and their ability to accommodate O vacancies. High-temperature ^{119}Sn NMR reveals that the O ions are mobile above 400 °C, oxygen mobility being required to hydrate these materials. The high protonic mobility, even in the high Y-content materials, is ascribed to the Y−O−Sn cation ordering, which prevents proton trapping on the more basic Y−O−Y sites.

INTRODUCTION

One approach to lowering the operation temperature of a solid oxide fuel cell (SOFC) involves the use of ceramic electrolytes that rely on protonic rather than O anion conduction to transfer charges between electrodes. Stable proton-conducting phases discovered to date include promising perovskite-based materials such as $BaZr_{1-x}M_xO_{3-x/2}$, $BaCe_{1-x}M_xO_{3-x/2}$, and $SrCe_{1-x}M_xO_{3-x/2}$ where M is a large trivalent ion.[1] Generally, the highest conductivity values are obtained for low M^{3+} substitution levels, typically between 5 and 20%. The case of $BaSn_{1-x}Y_xO_{3-x/2}$ is more unusual as very high conductivities have been obtained at the exceptionally high dopant concentration of $x = 0.50$.[1,2] Although the $BaSn_{1-x}Y_xO_{3-x/2}$ phases reach conductivities that are comparable to those of $BaZr_{1-x}Y_xO_{3-x/2}$[1,2] and are stable under CO_2 and H_2O atmospheres, studies of these compounds are rare. In all of these potential protonic conductors, substitution of the M^{4+} cations by subvalent M^{3+} dopants introduces charge compensating oxygen vacancies with concentrations of up to 8.3% of all the O sites in the case of $BaSn_{0.50}Y_{0.50}O_{2.75}$. The subsequent incorporation of protons proceeds by the reaction of oxygen vacancies with H_2O molecules, leading to the formation of OH groups.

The pure $BaSnO_3$ phase crystallizes in a cubic perovskite (ABO_3) structure with space group $Pm\bar{3}m$.[3] Yttrium can

Received: May 15, 2012
Published: June 13, 2012

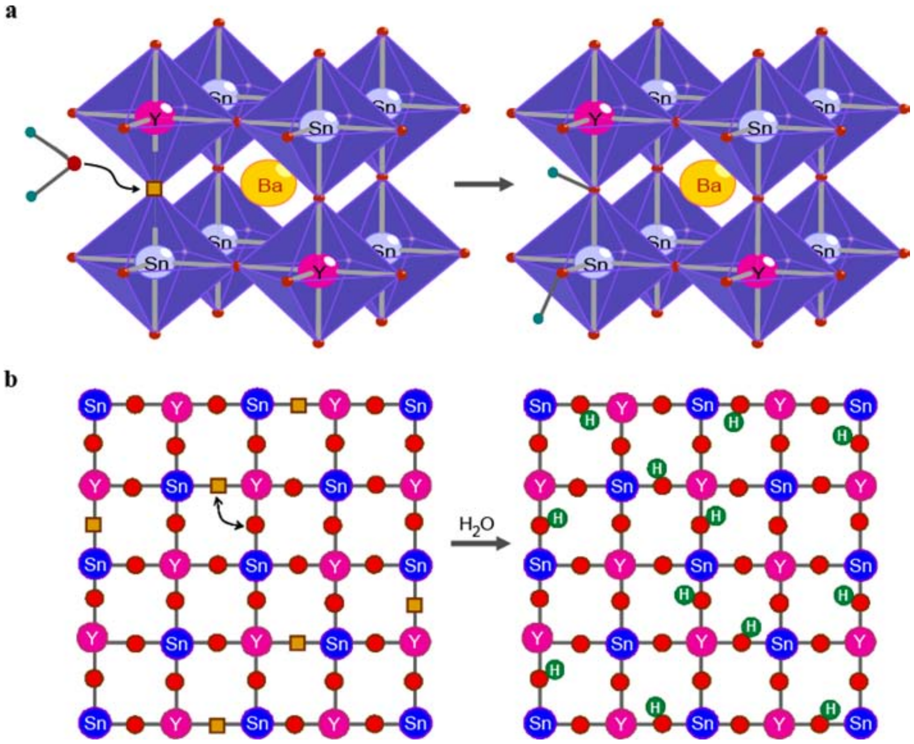

Figure 1. Structure of $BaSn_{1-x}Y_xO_{3-x/2}$. (a) Schematic representation of the hydration process by the reaction of a water molecule with a lattice O site and vacancy forming two hydroxyl groups, i.e. protonic defects. (b) Proposed structure for dry and hydrated $BaSn_{0.50}Y_{0.50}O_{2.75}$ with complete ordering of B-site cations. Barium atoms are omitted for clarity. The double-headed arrow shows a migration of an oxygen atom into a vacant site, leading to the conversion of one six-coordinated Sn site into a five-coordinate Sn cation (and vice versa) and resulting in two Sn atoms with average coordination numbers of 5.5 on the time scale of the migration. Yellow, blue, purple, red, and green spheres represent Ba, Sn, Y, O, and H atoms, respectively; yellow squares represent the oxygen vacancies.

substitute for tin on the B site, leading to the solid-solution $BaSn_{1-x}Y_xO_{3-x/2}$, where the end-member $BaSn_{0.50}Y_{0.50}O_{2.75}$ again adopts a cubic perovskite structure (Figure 1a). In some of the previously obtained X-ray diffraction patterns weak reflections were, however, observed in addition to those expected for a cubic perovskite; these superstructure reflections were ascribed to Y^{3+} and Sn^{4+} ordering on the B site which results in an $A_2BB'O_6$ superstructure (a double perovskite) involving a doubling of the ABO_3 unit cell.[2,4−6] The local structures occurring in these materials remain unclear since the intensities of the superlattice reflections are noticeably weaker than predicted for the fully ordered structure, indicating only partial Y/Sn ordering. Furthermore, no structural studies have been reported on materials with intermediate Y contents. On hydration, the O vacancies formed due to Y substitution are filled by OH groups, but the underlying cation sublattice presumably remains unchanged in terms of the degree of Y/Sn ordering (Figure 1a,b).

In this study, we investigate the local structure of $BaSn_{1-x}Y_xO_{3-x/2}$ by combining experimental NMR with DFT total energy and NMR calculations. We aim to gain insight into the structures and energetics of different distributions of Y dopants and O vacancies across a broad range of stoichiometries. The structures of cation sublattices and the locations of vacancies control the energetics and local structures of the hydroxyl groups in the hydrated phase. Thus, a study of local structure should ultimately contribute to an understanding of the high proton conductivities achieved in the hydrated phases. NMR spectroscopy is an ideal technique with which to investigate local structure in this material, since it is sensitive to details of local environment such as coordination number, site symmetry, and degree of distortion. In these complex materials with high vacancy contents, however, sites possessing atypical local environments and coordinations must be present, leading to difficulties in interpreting the spectra obtained. DFT calculations of optimized structures, total energies, and NMR parameters [the latter within the previously successful gauge-including projector augmented wave (GIPAW) approach[7,8]] can be of great assistance in this regard, yielding not only a direct interpretation of the experimental NMR but also new insights into the varied local structures occurring, as shown recently[9] for the related Sr- and Mg-doped $LaGaO_3$ systems.[10,11]

The local environments of relevant species can be individually probed by acquiring the spectra for all the NMR-active nuclei present in the solid, i.e., ^{119}Sn, ^{17}O, and ^{89}Y in the current $BaSn_{1-x}Y_xO_{3-x/2}$ phases, the subsequent assignments being assisted by the DFT calculations. ^{119}Sn is a spin $I = {}^1/_2$ nucleus (8.6% abundant) and is used here primarily to identify the distribution of Y in the materials, given that the ^{119}Sn nucleus is sensitive to the identity of the neighboring cations.[12,13] Furthermore, the presence of O vacancies adjoining the Sn sites should also be readily observable, since the vacancies lower the Sn coordination number leading to a change of chemical shift.[12] The spectra of both dry and hydrated samples were acquired in this work, both to assign the resonances and to assist in determining the distribution of O vacancies in the dry phases. ^{17}O (spin $I = {}^5/_2$, quadrupolar, 0.037% natural abundance) NMR was then used to confirm the cation ordering observed by ^{119}Sn NMR, as its shift is also sensitive to the identity of neighboring cations.[14,15] Finally, ^{89}Y (spin $I = {}^{1}/_{2}$, 100% natural abundance) spectra were acquired to determine whether any substitution on the perovskite A sublattice occurs; this is particularly important because this substitution acts to reduce the concentration of O vacancies (denoted as $V_O^{\bullet\bullet}$ in the Kröger–Vink notation).[16] For example, equal substitution on the A and B sites, i.e., $(Ba_{1-y}Y_y)_A(Sn_{1-y}Y_y)_BO_3$, where Y substitutes for both Sn (yielding sites denoted as Y'_{Sn})[16] and Ba ($Y^{\bullet}_{Ba}$), is self-compensating, and results in a stoichiometric O sublattice. A-site substitution can be driven by BaO loss during sintering as reported by Yamazaki et al. for the Y-substituted $BaZrO_3$ system.[17] Finally, high-temperature ^{119}Sn MAS NMR spectroscopy was used to explore the mobility of the vacancies in the lattice, the latter being required for the incorporation of water into the solid.

■ MATERIALS AND METHODS

Experimental Section. *Sample Preparation.* $BaSn_{1-x}Y_xO_{3-x/2}$ (x = 0.10, 0.20, 0.30, 0.40, and 0.50) samples were synthesized by a glycine-nitrate combustion route[18] using $Ba(NO_3)_2$ (Alfa Aesar, 99.999%), SnO_2 (Fisher Scientific, 99.40%), $Y(NO_3)_3{\cdot}6H_2O$ (Alfa Aesar, 99.9%), and glycine (Alfa Aesar, 99.7%) as starting materials. Stoichiometric ratios of the reactants were mixed in a small amount of deionized water with a nitrate to glycine ratio of 2:1. Mixtures were then dehydrated on a hot plate and auto-ignition resulted. Powders were ground and fired at 1200 °C for 10 h, pressed into pellets, buried in $BaZrO_3$ powder to prevent Ba evaporation, and sintered at 1600 °C for another 10 h. Hydration of the powders was performed in a tube furnace. The powders were first dried at 1000 °C for 2 h and then cooled in steps of 100 °C every 2 h until the temperature reached 200 °C, with wet N_2 flowing over the samples at a rate of 60 mL·min^{-1}. The previous cycle was repeated once with cooling from 800 to 200 °C so as to increase the hydration level of the powders. ^{17}O enrichment was performed by heating the dried samples (12 h at 950 °C under vacuum) in 50% ^{17}O-enriched $^{17}O_2$ gas (Isotec, 99%, used as received) for 2 days at 950 °C. The purity of the various compounds synthesized as above was checked by X-ray diffraction (XRD) using a Scintag diffractometer with Cu Kα radiation, with subsequent comparisons to diffraction patterns in the Joint Committee on Powder Diffraction Standards database (JCPDS 06-0399). Hydration levels were estimated by thermogravimetric (TGA) analyses using a Q500 TA Instruments under dry N_2 atmosphere.

^{119}Sn NMR Spectroscopy. ^{119}Sn NMR spectra were acquired at 11.7 T on a wide-bore Oxford 500 MHz Varian Infinity Plus spectrometer using a 3.2 mm HX Chemagnetics probehead tuned to 186.26 MHz. The samples were dried at 950 °C overnight prior to the experiments and then packed under an N_2 atmosphere in 3.2 mm zirconia rotors, which were then spun at a spinning frequency ν_r = 20 kHz. ^{119}Sn single-pulse experiments on dry samples were carried out using a $\pi/2$ pulse width of 2 μs (i.e., at an rf field amplitude of ν_1^{Sn} = 125 kHz) and a recycle delay of 70 s allowing full relaxation of the ^{119}Sn spins. Similar experimental conditions were used for the hydrated samples, save for a shorter recycle delay of 30 s. High-temperature ^{119}Sn MAS NMR experiments upon $BaSn_{0.50}Y_{0.50}O_{2.75}$ were performed on an 8.45 T wide-bore Varian Oxford Infinity Plus 360 MHz spectrometer equipped with a 7 mm HX high-temperature MAS probe from Doty Scientific, Inc. tuned to 134.18 MHz. The sample was packed in a boron nitride BN insert that was then placed in a 7 mm silicon nitride Si_3N_4 rotor. Spinning was performed under N_2 at ν_r = 4 kHz at room temperature and at ν_r = 6 kHz above 200 °C. Temperature calibration of the probe was carefully performed by using the ^{207}Pb resonance of $Pb(NO_3)_3$[19,20] below 400 °C and the ^{119}Sn resonance of $Pr_2Sn_2O_7$[21] above 400 °C. The temperatures given in the text correspond to actual sample temperatures with an estimated accuracy of ±4 °C. One-pulse spectra were recorded with a $\pi/2$ pulse width of 5 μs at ν_1^{Sn} = 50 kHz and a recycle delay of 3 s. Chemical shifts were externally referenced to SnO_2 at −604.3 ppm.

^{17}O NMR Spectroscopy. ^{17}O NMR experiments were carried out on a 14.1 T wide bore Bruker Avance 600 MHz spectrometer equipped with a 4 mm HX probehead operating at 81.36 MHz. All samples were packed inside 4 mm MAS zirconia rotors and spun at ν_r = 15 kHz. ^{17}O one-dimensional spectra were recorded using rotor-synchronized Hahn echo experiments with an evolution period τ_r of one rotor period to avoid probe ringing. $\pi/6$ and $\pi/3$ pulses were used with an rf field amplitude of ν_1^{O} = 100 kHz (the $\pi/6$ and $\pi/3$ pulse lengths corresponding to those measured for liquid $H_2{}^{17}O$). Two-dimensional triple-quantum MAS NMR experiments were performed using the z-filtered pulse sequence.[22] Hard and soft pulses were performed at ν_1^{O} = 100 kHz and approximately 15 kHz, respectively. The multiple-quantum transfer was optimized for every sample to increase the excitation efficiency of the MQ coherences. The t_1 increment was rotor-synchronized to one rotor period of 66.67 μs at ν_r = 15 kHz. The recycle delay was set to 5 s for all experiments. The chemical shift was externally referenced to water at 0.0 ppm. The signal observed at approximately 380 ppm corresponds to either ^{17}O enrichment of the ZrO_2 rotor or possibly to remnant $BaZrO_3$ powder from the sintering, these materials resonating at 378[23] and 376[15] ppm, respectively.

^{89}Y NMR Spectroscopy. ^{89}Y NMR experiments for the dry samples were performed at 11.7 T on a wide-bore Oxford 500 MHz Varian Infinity Plus spectrometer equipped with a 7.5 mm HX Chemagnetics probehead tuned to 24.50 MHz. The samples were prepared as described above and were packed in 7.5 mm silicon nitride Si_3N_4 rotors and spun at a spinning frequency of 4 kHz. ^{89}Y single-pulse experiments were carried out using a $\pi/6$ pulse width of 4 μs (the shorter $\pi/6$ pulse being used, this pulse length representing the most efficient way to collect data from nuclei with long spin–lattice relaxation (T_1) values, i.e., ^{89}Y), at an rf field amplitude of ν_1^{Y} = 20 kHz and recycle delays of 250 s. High-field ^{89}Y NMR experiments on the hydrated materials were performed at 19.6 T on a ultra-narrow-bore Bruker DRX 830 MHz spectrometer at the National High Magnetic Field Laboratory, Tallahassee, Florida, United States, using a 7 mm single-channel probe tuned to 40.84 MHz. All samples were packed inside 7 mm Si_3N_4 rotors and spun at ν_r = 8 kHz. The chemical shift was externally referenced to the most intense resonance of Y_2O_3 at 330 ppm.

NMR Analyses. MatLab and MatNMR[24] were used to process the data and perform the deconvolutions. ^{119}Sn deconvolutions across the whole series used fixed chemical shifts obtained from an initial deconvolution. Simulations were performed using SIMPSON[25] and standard numerical techniques.[26]

Computational Methods. *Energetics and Configurations.* The first principles computational methods used here are very similar to those adopted in our recent studies of oxides and gallates,[27] Mg-doped $LaGaO_3$,[9] and similar studies of Sn- and Y-bearing pyrochlores.[13,28] Briefly, fully periodic calculations of NMR parameters within the gauge-including projector augmented wave (GIPAW) method[7,8] have been performed using the CASTEP code,[29] including electric field gradient tensors and associated quadrupolar interaction parameters for ^{17}O sites.[30] The Perdew–Burke–Ernzerhof GGA-type exchange-correlation functional has been used throughout.[31] All structures have been fully geometry optimized prior to the NMR calculations with tolerances 1×10^{-6} eV, 1×10^{-3} eV/Å, 1×10^{-3} Å, and 5×10^{-3} GPa for total energy, maximum atomic force, maximum atomic displacement, and maximum cell stress tensor component, respectively, a basis set cutoff energy of 40 Ry, and Monkhorst–Pack **k**-point meshes of dimension 6×6×6, 3×3×3, and 2×2×2 for the perovskite primitive cell, 8 and 27 formula unit supercells, respectively. The PAW sets used for each element are detailed in the Supporting Information (SI).

A 3×3×3 supercell was considered for the x = 0.074 composition. For BB doping, two 'nn' configurations with Y dopants placed as nearest neighbor cations (nn) and three 'distant' configurations with Y separated as widely as possible within the supercell were calculated. Three 'ordered' configurations are also considered where Y atoms occupy next-nearest neighbor (nnn) positions. For AB doping in the same 3×3×3 supercell, we investigated two configurations with Y either nn or distant with respect to each other. The BB-doped

Table 1. Range in Doping Energies (kJ/mol per Y) Relative to the Ground State at Each Stoichiometry, Formation Energies of the Ground State (kJ/mol) Relative to BaO, Y_2O_3, and SnO_2, and Effective Perovskite Unit Lattice Constants, All As a Function of Y Content[a]

x	relative doping energy per Y (kJ/mol)				E_{form}[b] (kJ/mol), a_{latt}[b] (Å)
	BB-doped			AB-doped	
	$Sn{-}V_O^{\bullet\bullet}{-}Sn$	$Y'_{Sn}{-}V_O^{\bullet\bullet}{-}Sn$	$Y'_{Sn}{-}V_O^{\bullet\bullet}{-}Y'_{Sn}$		
0.000	—	—	—	—	−95.3, 4.180
0.074	0−12 [4], 32[c] [1]	1−5 [2]	2 [1]	32−37 [2]	−89.0, 4.202
0.250	0−59 [7]	19−52 [4]	38 [1]	43 [1]	−79.1, 4.248
	‘ordered’	‘antisite’	‘planar’		
0.500	0−19 [6]	15[d] −40 [10]	13[e] [1], 42−80 [11]	19−28 [3]	−56.7, 4.291

[a] The number of each type of configuration is shown in square brackets. [b] Computed from the GS obtained at each stoichiometry. [c] $Y'_{Sn}{-}O{-}Y'_{Sn}$, with the vacancy coordinated to two Sn atoms ($Sn{-}V_O^{\bullet\bullet}{-}Sn$) and distant from the two Y dopants. [d] ($Y'_{Sn}{-}V_O^{\bullet\bullet}{-}Y'_{Sn}$) + ($Sn{-}V_O^{\bullet\bullet}{-}Sn$) configuration. [e] $2\times(Y'_{Sn}{-}V_O^{\bullet\bullet}{-}Y'_{Sn})$ configuration.

configurations investigated for $x = 0.25$ (two Y'_{Sn} and $V_O^{\bullet\bullet}$ in a 2×2×2 supercell), consist of six ‘nn’, two ‘distant’, and four ‘ordered’ configurations (defined as above), along with a single nn AB-doped ($Y_{Ba}^{\bullet}$ and Y'_{Sn} in a 2×2×2 supercell) configuration. Finally, the BB-doped configurations considered at $x = 0.5$ (four Y'_{Sn} and two $V_O^{\bullet\bullet}$ in a 2×2×2 supercell) comprise six ‘ordered’ configurations where each Y cation neighbors only Sn cations, ten ‘antisite’ configurations obtained by the swapping of a single Sn−Y pair in the ordered arrangement, and twelve ‘planar’ configurations in which the (100) B-sublattice supercell planes are each fully occupied by Y or Sn in alternating succession. In addition, three AB-doped $x = 0.5$ configurations (two $Y_{Ba}^{\bullet}$ and two Y'_{Sn} in a 2×2×2 supercell) are considered, namely nn, intermediate, and distant arrangements, characterized by a progressive increase in both the $Y_{Ba}^{\bullet}{-}Y_{Ba}^{\bullet}$ and $Y'_{Sn}{-}Y'_{Sn}$ separations. The ground state (GS) configuration was identified for each value of x and type of doping (BB vs AB) and cation/vacancy arrangements. The optimized structures of all configurations are considered are fully detailed in the SI.

The configurational energetics obtained across the range of stoichiometries may be meaningfully compared via the doping energies, defined as

$$\frac{1}{2}(Y_2O_3) + \frac{1}{x}(BaSnO_3) \rightarrow Ba_{(1/x)-(1/2)}Sn_{(1/x)-(1/2)}YO_{3/x} + \frac{1}{2}(BaO) + \frac{1}{2}(SnO_2) \qquad \text{(AB doping)} \tag{1}$$

$$\frac{1}{2}(Y_2O_3) + \frac{1}{x}(BaSnO_3) \rightarrow Ba_{1/x}Sn_{(1/x)-1}YO_{(3/x)-(1/2)} + SnO_2 \qquad \text{(BB doping)} \tag{2}$$

where the doping energies presented in Table 1 are all quoted per Y dopant introduced and are relative to the ground state (lowest doping energy, either AB- or BB-doped) obtained for each stoichiometry. The phase equilibria above have been selected for their relevance to the method used to synthesize these materials. The energies of formation relative to binary oxides were also computed (Table 1) and are defined as

$$\frac{x}{2}(Y_2O_3) + \left(1 - \frac{x}{2}\right)(BaO) + \left(1 - \frac{x}{2}\right)(SnO_2) \rightarrow Ba_{1-(x/2)}Sn_{1-(x/2)}Y_xO_3 \qquad \text{(AB doping)} \tag{3}$$

$$\frac{x}{2}(Y_2O_3) + BaO + (1 - x)(SnO_2) \rightarrow BaSn_{1-x}Y_xO_{3-(x/2)} \qquad \text{(BB doping)} \tag{4}$$

per mole of perovskite equivalent units, taking the lowest doping energy (either AB- or BB-doped) obtained for each stoichiometry as representative of the doped supercell.

NMR Calculations. The single-point NMR calculations used the same **k**-point meshes as used in the initial structure optimization but with a larger cutoff energy of 50 Ry. The isotropic magnetic shieldings (σ_{iso}) were converted to the shifts (δ_{iso}) to allow comparison with experimental values via the shielding references computed in our previous work for ^{17}O, $\delta_{iso}(^{17}O) = 223.7 - 0.8880\sigma_{iso}(^{17}O)$ where we obtained a mean absolute error (MAE) of 12 ppm relative to experiment over a range of materials;[27] for ^{89}Y the following expression, $\delta_{iso}(^{89}Y) = 2385.30 - 0.8945\sigma_{iso}$ (MAE = 15 ppm) was derived from a refit of the model compound results of Reader et al. with a free gradient),[28] whereas for ^{119}Sn, $\delta_{iso}(^{119}Sn) = 2123.0 - 0.8840\sigma_{iso}$ (MAE = 55 ppm) was derived from a refit of the results of Mitchell et al.[13] The shielding and EFG tensor conventions used are detailed in the SI, along with a full presentation of all computed NMR data. The NMR parameters discussed below, however, represent only the lowest-energy AB- and BB-doped configurations obtained for each stoichiometry, along with the first higher-energy BB-doped configuration with at least one five-fold-coordinated Y cation (the higher energy BB-doped configuration is included in the case of the $x = 0.5$ phase). Beyond the NMR parameters obtained from optimized low-energy configurations, the effects of variation in lattice constant upon the computed ^{119}Sn and ^{89}Y shifts have also been explored, as discussed below and in more detail in the SI.

■ RESULTS AND DISCUSSION

Optimized Structures and Energetics. Prior to the discussion of the experimental results, the DFT optimized structures and energetics at $x = 0$, 0.074, 0.25, and 0.5 are considered, as fully detailed in the SI. The intensive nature of the calculations makes the full determination of all symmetry-distinct configurational structures and energies in each doped supercell impractical, but a reasonably broad sampling of structures was achieved. For BB doping, i.e., the substitution of two Y atoms for Sn onto the B site Y'_{Sn} and the formation of one O vacancy $V_O^{\bullet\bullet}$, a variety of configurations were explored with different $Y'_{Sn}{-}Y'_{Sn}$ separations. For the $x = 0.074$ and 0.25 ‘nn’ configurations, Y dopants were placed as nearest neighbor cations (nn); for the ‘distant’ configurations, Y atoms were separated as widely as possible within the supercell (‘distant’ configurations), while for the ‘ordered’ configurations, the Y atoms occupy next-nearest neighbor (nnn) positions (forming Y−Sn−Y contacts (ignoring the intervening oxygen and vacancies)). A series of configurations were then generated as a function of the relative position of the vacancy(ies). For AB doping only nn and distant configurations were explored, and fewer configurations were required since the substitution of two Y atoms for one Sn and one Ba atom, $Y_{Ba}^{\bullet}$ and Y'_{Sn} is not accompanied by vacancy formation. For $x = 0.5$, ‘ordered’ configurations were chosen to explore the previous diffraction observation of a degree of Y/Sn ordering at $x = 0.5$,[2] in which each Y cation neighbors only Sn cations. 'Antisite' and 'planar' configurations were then obtained by either swapping a single Sn−Y pair in the ordered arrangement or occuping the (100) B-sublattice supercell planes by Y or Sn in alternating succession. The ground state (GS) configuration was identified for each value of x and type of doping (BB vs AB) and arrangement of cations and vacancy.

Table 1 contains the phase formation energies and relative doping energies obtained at each Y content, where the latter have been classed according to the $\mathrm{Y}'_{\mathrm{Sn}}/\mathrm{V}_{\mathrm{O}}^{\bullet\bullet}$ or $\mathrm{Y}_{\mathrm{Ba}}^{\bullet}/\mathrm{Y}'_{\mathrm{Sn}}$ arrangement. As in Mg-doped $\mathrm{LaGaO_3}$,[9] the introduction of aliovalent dopants and compensating vacancies into $\mathrm{BaSnO_3}$ (BB doping) leads to a progressive destabilization of the lattice, the gradient $\partial E_{\mathrm{form}}/\partial x$ computed here at +76 kJ/(mol Y) being slightly lower than the value +84 kJ/(mol Mg) obtained for Mg-doped $\mathrm{LaGaO_3}$.[9] The similar gradient computed for self-compensated AB doping is significantly higher at +95 kJ/(mol Y). In support of the present methods, we note that the formation energy of pure $\mathrm{BaSnO_3}$ computed here at −95 kJ/mol is very similar to the value −93 kJ/mol provided by the recent DFT study of Bévillon et al.[32] Doping leads to progressive lattice dilation (Table 1), the computed gradient $\partial a_{\mathrm{latt}}/\partial x = 0.22$ Å/(mol Y) being in satisfactory agreement with the experimental value of 0.27 Å/(mol Y).[33] The theoretical lattice constants overestimate experiment by amounts ranging from 1.1 to 1.7% of the latter, an error of typical size for pure DFT methods.

Focusing on the most dilute $x = 0.074$ phase, the GS, shown in Figure 2a, comprises a $\mathrm{Sn{-}V_{O}^{\bullet\bullet}{-}Sn}$ 'ordered' configuration where the vacancy is nnn to both Y dopants, confirming the results of previous charged cell DFT calculations (one $\mathrm{Y}'_{\mathrm{Sn}}$ and $\mathrm{V}_{\mathrm{O}}^{\bullet\bullet}$ in a 2×2×2 supercell) in which nnn $\mathrm{Y}'_{\mathrm{Sn}}{-}\mathrm{V}_{\mathrm{O}}^{\bullet\bullet}$ trapping was found to be favored over both nn and more distant arrangements.[34] Another interesting finding is that the $\mathrm{Y}'_{\mathrm{Sn}}{-}\mathrm{V}_{\mathrm{O}}^{\bullet\bullet}{-}\mathrm{Y}'_{\mathrm{Sn}}$ defect trimer is only +2 kJ/mol per Y higher than the GS, while the corresponding $\mathrm{Y}'_{\mathrm{Sn}}{-}\mathrm{O}{-}\mathrm{Y}'_{\mathrm{Sn}}$ configuration with $\mathrm{V}_{\mathrm{O}}^{\bullet\bullet}$ well separated from both dopants lies much higher at +32 kJ/mol per Y, indicative of a strong nn $\mathrm{Y}'_{\mathrm{Sn}}{-}\mathrm{Y}'_{\mathrm{Sn}}$ repulsion when dopants are not stabilized by an intervening vacancy. This is in keeping with the energetics for large $\mathrm{M^{3+}}$ dopants in $\mathrm{BaZrO_3}$ obtained by Björketun et al.,[35] where nn dopant arrangements were found to be strongly disfavored. It should be noted, however, that the majority of the configurations considered occur within a narrow range of doping energies of only +10 kJ/mol relative to the GS, indicative of the potential for a high degree of disorder. It is also clear that BB doping is favored over AB doping at this Y concentration within the phase equilibria considered (eqs 1 and 2). It is important to note that the A-sublattice Y cation ($\mathrm{Y}_{\mathrm{Ba}}^{\bullet}$) in the AB-doped configurations consistently moves off the center of the $\mathrm{YO_{12}}$ void, with implications for the ^{89}Y chemical shift that will be discussed below. In the facial-bonding arrangement (Figure S1a, SI), the $\mathrm{Y^{3+}}$ ion associates more closely with four O ions at distances 2.40−2.43 Å, and two further sets of four ions at 2.63−2.69 Å and 3.56−3.63 Å; and in the corner-bonding arrangement (Figure S1b, SI), the cation binds to a first group of six O ions at distances 2.37−2.43 Å, and two further sets of three oxygen ions at 3.29−3.42 Å and 3.50−3.59 Å, all as compared with an optimized Ba−O distance of 2.96 Å in pure $\mathrm{BaSnO_3}$.

Examining the higher Y content configurations, the ground state at $x = 0.25$ (Figure 2b), corresponds to a $\mathrm{Sn{-}V_{O}^{\bullet\bullet}{-}Sn}$ 'distant' configuration, where, as shown above for $x = 0.074$, the vacancy is located as nnn (i.e., 'distant') to the Y cations. Broadly, the BB-doped configurational energies may be classed according to the proximity of Y dopants to each other, the 'distant' and 'ordered' structures (i.e., those with Y−O−Sn−O−Y linkages) falling in the combined range 0 to +38 kJ/mol, and those with two nearby Y atoms (i.e., $\mathrm{Y}'_{\mathrm{Sn}}{-}\mathrm{O}{-}\mathrm{Y}'_{\mathrm{Sn}}$ configurations) in the range from +38 to +59 kJ/mol, again in keeping with strong nn $\mathrm{Y}'_{\mathrm{Sn}}{-}\mathrm{Y}'_{\mathrm{Sn}}$ repulsion. The single calculated nn AB-doped configuration occurs at +43 kJ/mol, confirming that BB doping is preferred at this Y concentration within the phase equilibria considered (eqs 1 and 2). Finally, for $x = 0.5$, the highest Y content considered, the ground state shown in Figure 2c consists of an 'ordered' Y/Sn arrangement where in all the vacancies experience a $\mathrm{Y}'_{\mathrm{Sn}}{-}\mathrm{V}_{\mathrm{O}}^{\bullet\bullet}{-}\mathrm{Sn}$ environment and occupy nnn positions with respect to each other. The high defect concentration at $x = 0.5$ makes a classification of the configurations according to dopant separations more useful than the dopant/vacancy arrangements used above. Table 1 shows that, broadly speaking, the 'ordered' Y/Sn arrangement is more stable than either 'antisite' or 'planar' arrangements. This is likely due to the fact that the latter two arrangements lead to

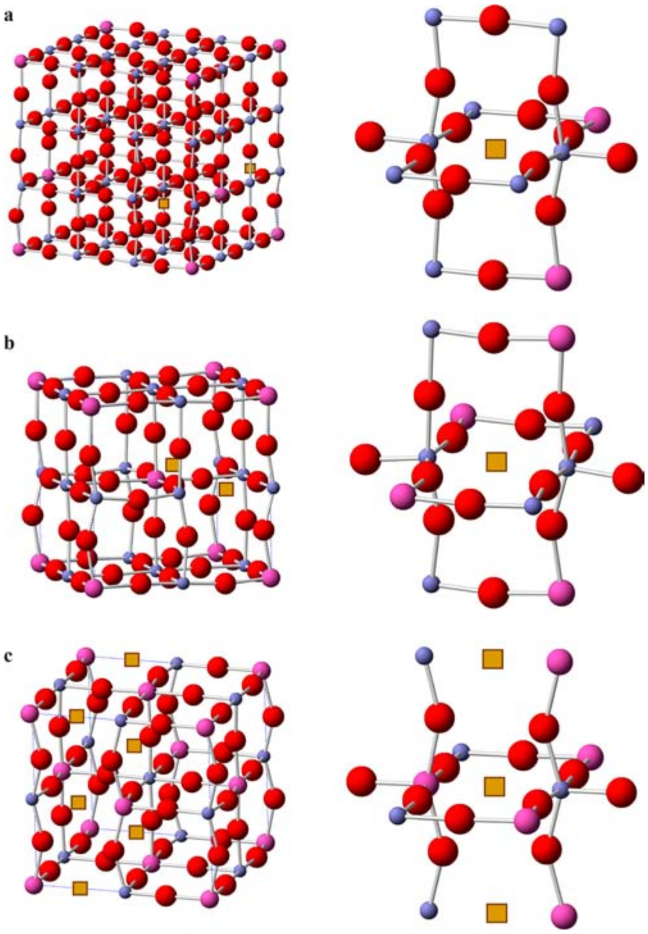

Figure 2. Optimized GS configurations (left) and local vacancy environments (right) for (a) $x = 0.074$, (b) $x = 0.25$, and (c) $x = 0.5$ (the two $\mathrm{V}_{\mathrm{O}}^{\bullet\bullet}$ centers in the supercell are equivalent in this case). Red, pink, and blue spheres and yellow squares denote O, Y, Sn, and $\mathrm{V}_{\mathrm{O}}^{\bullet\bullet}$, respectively. Ba cations have been omitted for clarity. Vacancies are located between two Sn cations and nnn to two or more Y cations in (a) and (b), whereas in (c), the vacancies are located between Y and Sn sites in a cation-ordered structure.

an increase in the degree of nn $Y'_{Sn}-Y'_{Sn}$ repulsion in the lattice, given that each Y ion in the ordered, antisite, and planar arrangements interacts with, on average, zero, two, and four nn Y, respectively. The finding from the previous diffraction study that some degree of Y/Sn ordering is favored in the $x = 0.5$ phase[2] is therefore confirmed by the present calculations. However, some degree of cation disorder on the B-sublattice is still anticipated, given that a small number of configurations such as the planar 2 × ($Y'_{Sn}-V_O^{\bullet\bullet}-Y'_{Sn}$) and antisite ($Y'_{Sn}-V_O^{\bullet\bullet}-Y'_{Sn}$) + ($Sn-V_O^{\bullet\bullet}-Sn$) structures have energies within a reasonable range of the ground state (+13 and +15 kJ/mol per Y, respectively) and are likely to be accessible at synthesis temperatures.

XRD. In order to investigate cation and vacancy ordering experimentally, we have studied both dry and hydrated solid solutions of $BaSn_{1-x}Y_xO_{3-x/2}$ with x values ranging from 0.10 to 0.50. Figure 3 shows the diffraction pattern for nominally dry $BaSn_{1-x}Y_xO_{3-x/2}$ ($0.10 \le x \le 0.50$). The powders adopt a cubic perovskite structure, space group $Pm\bar{3}m$, across the range of compositions, the cell parameter increasing with Y substitution level. Yttria (Y_2O_3) is the most common impurity occurring in these materials but was not detected in the present samples. In addition, no extra reflections are observed at low angles, as would be expected if long-range cation ordering were present, notionally leading to a double perovskite superstructure ($2a_p \times 2a_p \times 2a_p$ supercell, a_p = perovskite unit cell length) with $Fm\bar{3}m$ symmetry.[36] Thus, if any ordering is present, it must be short ranged. The $x = 0.10$ phase contains a small fraction of the unsubstituted $BaSnO_3$ phase present as an impurity (as indicated by arrows).

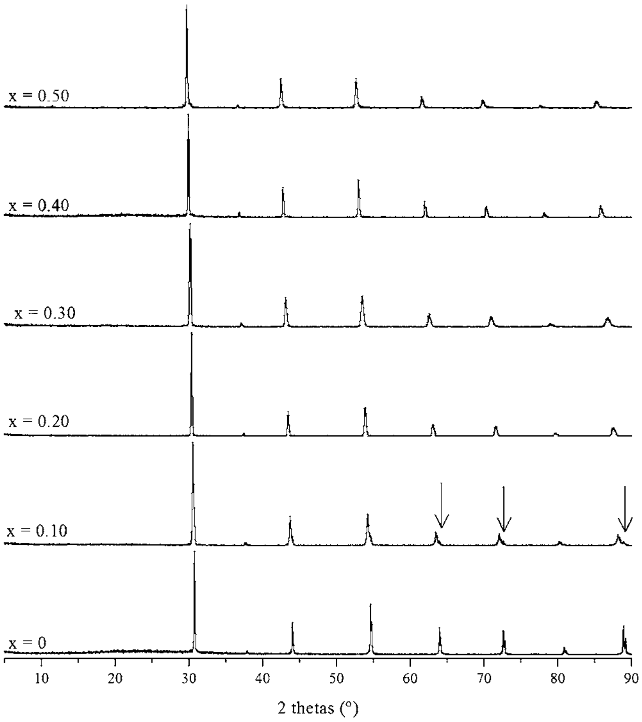

Figure 3. Powder X-ray diffraction patterns of $BaSn_{1-x}Y_xO_{3-x/2}$ for $0 \le x \le 0.50$. Shoulders (peaks) due to the Cu Kα_2 radiation are visible at high angles for $x = 0.0$. Arrows indicate reflections from a small fraction of unsubstituted $BaSnO_3$ present at $x = 0.10$.

TGA. The OH content associated with water loss at elevated temperature can be readily extracted from the TGA results for the hydrated $BaSn_{1-x}Y_xO_{3-x/2}(OH)_y$ samples (where $y \le x$; Figure 4). The concentration of protonic defects in the hydrated samples increases with level of Y substitution, as expected. All samples show a hydration level close to maximum, namely two OH groups to each O vacancy ($y \le x$), except in the case of $BaSn_{0.60}Y_{0.40}O_{2.80}$ where only a lower level of hydration could be achieved. We have repeated the hydration process a number of times for this sample, and the total water uptake was always significantly lower than the theoretical maximum. The small mass loss seen below 200 °C for the x = 0.10 and 0.50 samples is ascribed to the loss of surface water.

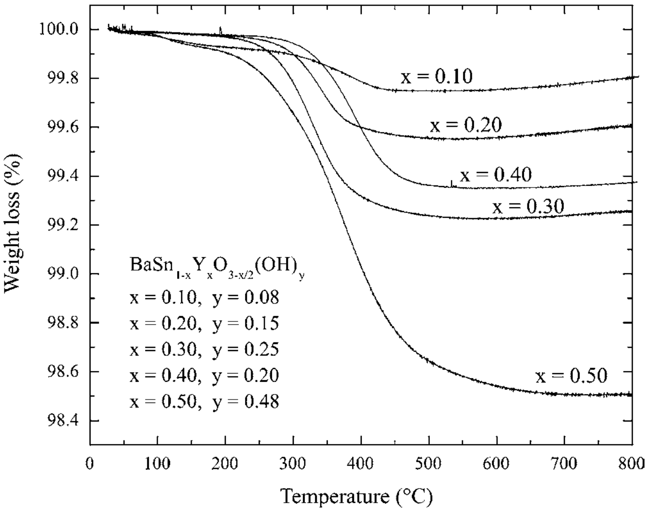

Figure 4. TGA data for $BaSn_{1-x}Y_xO_{3-x/2}(OH)_y$ ($y \le x$) in the range $0.10 \le x \le 0.50$. The protonic defect concentrations were calculated from the mass of water lost from room temperature to 800 °C.

^{119}Sn NMR. The ^{119}Sn MAS NMR spectrum of undoped $BaSnO_3$ (Figure 5a) contains a single, sharp resonance at −679 ppm from the octahedral $Sn(OSn)_6$ environment.[12] Two very different chemical shift regions are present in the spectra of the dry Y-substituted materials (Figure 5a). The first, between −550 and −700 ppm, contains a series of resonances, the number and intensities of these resonances varying sensitively with the Y doping level. In addition to the $Sn(OSn)_6$ peak, two further resonances at −645 and −618 ppm are seen in this region in the $BaSn_{0.90}Y_{0.10}O_{2.95}$ and $BaSn_{0.80}Y_{0.20}O_{2.90}$ spectra that can be tentatively assigned to Sn octahedra containing one and two Y cations, respectively, in their first cation coordination shells, i.e., $Sn(OSn)_5(OY'_{Sn})_1$ and $Sn(OSn)_4(OY'_{Sn})_2$. On the basis of this assignment, each Y ion doped into the Sn local shell shifts the resonance by approximately +27 to +34 ppm. Further higher frequency resonances are observed that can be ascribed to environments with higher numbers of neighboring Y cations as the Y substitution increases ($x \ge 0.30$), but it becomes more difficult to assign the new resonances to specific local environments due to increasing overlap, the shift observed per Y becoming smaller (Table S1 in the SI). The Sn local environments in $BaSn_{0.60}Y_{0.40}O_{2.80}$ differ radically from those observed in the more lightly doped phases, apparently segregating into environments rich and poor in Y with associated resonances at approximately −570 and −645 ppm, respectively. Only one broad resonance at −564 ppm is seen in this first region at $x = 0.5$, i.e. $BaSn_{0.50}Y_{0.50}O_{2.75}$, indicating that one local environment, tentatively assigned to $Sn(OY'_{Sn})_6$, dominates. A second experimental region becomes more clearly visible at higher substitution levels ($x \ge 0.20$) and contains only

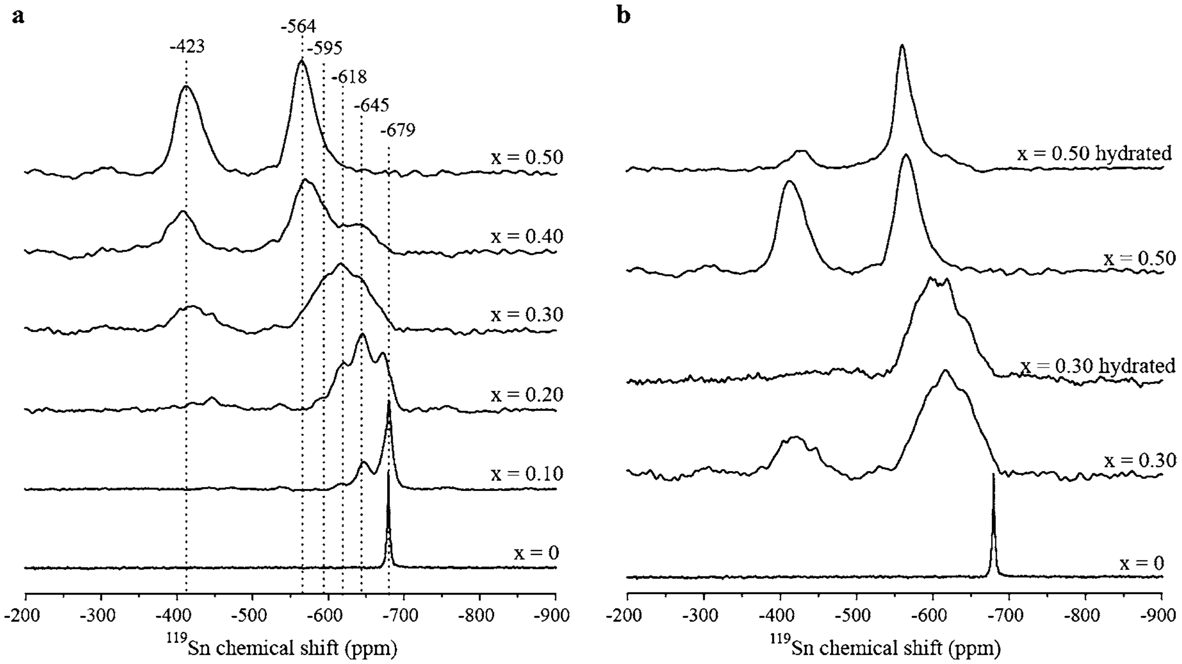

Figure 5. ^{119}Sn MAS NMR single-pulse spectra of $BaSn_{1-x}Y_xO_{3-x/2}$ samples. (a) Dry $BaSn_{1-x}Y_xO_{3-x/2}$. (b) Comparison between dry and hydrated samples for $BaSn_{0.30}Y_{0.70}O_{2.85}$ and $BaSn_{0.50}Y_{0.50}O_{2.75}$. The major resonances have been labeled with their isotropic chemical shifts.

one broad resonance at −423 ppm, which is assigned to five-coordinated Sn environments. Prior ^{119}Sn NMR studies of M_2SnO_3 (M = Li, Na, or K) materials by Clayden et al.[12] showed that the change from six- to five-fold Sn coordination in Sn(IV) materials lead to a shift of resonances to higher frequency by approximately +140 ppm, consistent with this assignment. The shift with coordination environment is quite general, a shift to higher frequencies on decrease of coordination number being well-established for ^{27}Al, ^{25} Mg, and ^{71}Ga cations, for example.[37]

In order to confirm the assignment of these resonances, the spectra of the dry and hydrated samples are compared (Figure 5b for $BaSn_{0.70}Y_{0.30}O_{2.85}$ and $BaSn_{0.50}Y_{0.50}O_{2.75}$, and Figure S2 in SI for all samples). On hydration, the resonance at −423 ppm disappears for $BaSn_{0.70}Y_{0.30}O_{2.85}$ while it is greatly reduced in the case of $BaSn_{0.50}Y_{0.50}O_{2.75}$, consistent with its assignment to a five-fold-coordinated $Sn(OX)_5(V_O^{\bullet\bullet}X)$ site. During the hydration process, the O vacancies are filled either by OH groups or O ions (Figure 1b), reducing the ratio of five- to six-fold-coordinated Sn cations in the structure. The residual resonance at −423 ppm in the hydrated $BaSn_{0.50}Y_{0.50}O_{2.75}$ is presumably due to incomplete hydration of the material, despite the fact that the TGA data (Figure 4) suggest that almost complete hydration is nominally achieved. This indicates that some of the water in $BaSn_{0.50}Y_{0.50}O_{2.75}$ is present as a surface species, which gives rise to the water loss seen between room temperature and approximately 200 °C in the TGA (Figure 4).

The concentration of the different local environments expected for a random distribution of Y and vacancies in the lattice can be readily calculated and compared with the experimental data using numerical simulations[24−26] (Figure 6, and Figure S3 and Table S1 in SI) to determine if there is any evidence for clustering and cation ordering. We focus on the six-fold-coordinated sites, given that a useful range of distinct environments can be resolved for these sites. The fractional intensity of the $Sn(OSn)_6$ resonance is compared with those of the z = 1, 2, and 3, $Sn(OSn)_{6-z}(OY'_{Sn})_z$ resonances, and with the sum of the z = 4, 5, and 6 resonances, so as to overcome the difficulty of extracting intensities from overlapping resonances and to provide a simpler and more reliable analysis. For substitution levels $x < 0.3$, the concentrations of Sn local environments remain close to those predicted for random doping (Figure 6a−e), while for $x \geq 0.3$, there is a clear tendency to form z = 4, 5, and 6 sites at concentrations in excess of those predicted for random doping (Figure 6e). The latter finding provides clear evidence for cation clustering or ordering in the more heavily doped phases. As discussed above, the simplest ordering scheme that may be envisaged for this system consists of an alternation of Sn and Y atoms on the B-sublattice (Figure 1b), leading to the prediction of a single $Sn(OY'_{Sn})_6$ environment at $x = 0.5$. This is consistent with the NMR spectrum of $BaSn_{0.50}Y_{0.50}O_{2.75}$, which is dominated by the $Sn(OY'_{Sn})_6$ resonance at −564 ppm, indicating that the material displays a high degree of local ordering. Furthermore, this ordering scheme was shown to be favored over the other cation arrangements within the DFT calculations above (Table 1). The extension of this ordering to long-range should lead experimentally to superlattice reflections indexable to the space group $Fm\bar{3}m$ in the XRD pattern. Although the present XRD measurements (Figure 3) do not reveal additional reflections of this type, they have been observed in previous studies, albeit with intensities significantly lower than would be predicted for full ordering.[4,5,36] For $BaSn_{0.60}Y_{0.40}O_{2.80}$, while the $Sn(OY'_{Sn})_6$ resonance again dominates (along with a shoulder attributed to environments such as $Sn(OSn)(OY'_{Sn})_5$) the presence of a broad resonance at lower frequencies due to Y-poor environments suggests that the material comprises Sn-rich clusters within an overwhelmingly Y/Sn alternating ordered network. The transition from structural disorder to order from low to high Y doping levels appears to occur via a two-phase process: one phase being Y rich and ordered, and the second, Y poor and disordered. The onset of the two-phase process is evident in $BaSn_{0.70}Y_{0.30}O_{2.85}$, where higher concentrations of $Sn(OSn)_2(OY'_{Sn})_4$, $Sn(OSn)_1(OY'_{Sn})_5$, and $Sn(OY'_{Sn})_6$ environ-

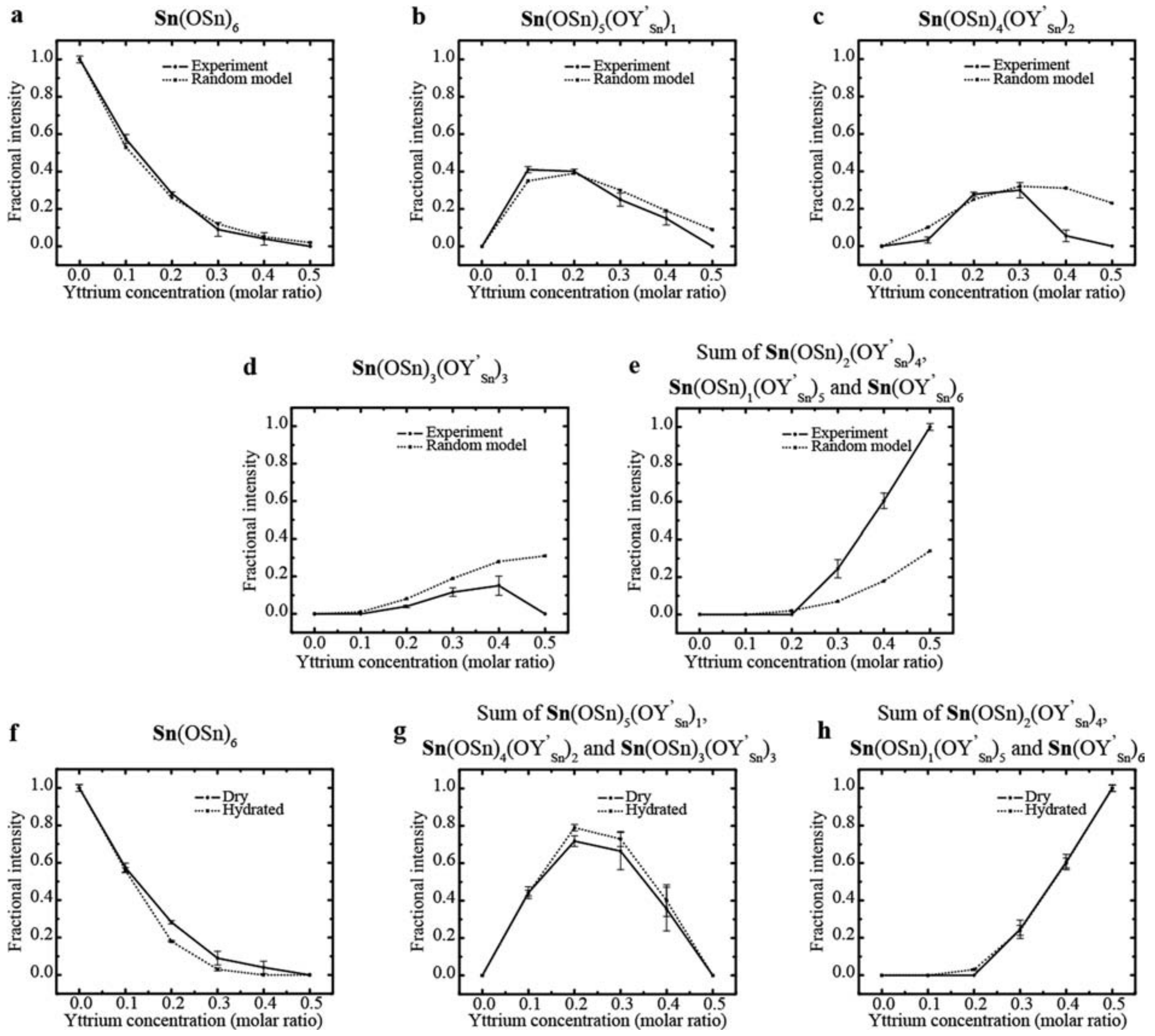

Figure 6. Comparison between the observed fractional intensities of distinct $Sn(OSn)_{6-z}(OY'_{Sn})_z$ local environments and those calculated assuming a random distribution of Y on the Sn sublattice, as a function of Y-doping level. Dry samples: Intensities of (a) $\mathbf{Sn}(OSn)_6$; (b) $\mathbf{Sn}(OSn)_5(OY'_{Sn})_1$; (c) $\mathbf{Sn}(OSn)_4(OY'_{Sn})_2$; (d) $\mathbf{Sn}(OSn)_3(OY'_{Sn})_3$; (e) sum of $\mathbf{Sn}(OSn)_2(OY'_{Sn})_4$, $\mathbf{Sn}(OSn)_1(OY'_{Sn})_5$, and $\mathbf{Sn}(OY'_{Sn})_6$. Comparison between the intensities found in the dry and hydrated samples: (f) $\mathbf{Sn}(OSn)_6$; (g) sum of the $\mathbf{Sn}(OSn)_5(OY'_{Sn})_1$, $\mathbf{Sn}(OSn)_4(OY'_{Sn})_2$, and $\mathbf{Sn}(OSn)_3(OY'_{Sn})_3$ environments; (h) sum of the $\mathbf{Sn}(OSn)_2(OY'_{Sn})_4$, $\mathbf{Sn}(OSn)_1(OY'_{Sn})_5$, and $\mathbf{Sn}(OY'_{Sn})_6$ environments.

ments occur than are predicted for random doping. The coexistence of two domains with different compositions and local structures may be one reason why the $x = 0.4$ material is difficult to hydrate fully; it is possible that trapping at domain boundaries could hinder the diffusion of water (dissociated to form protons and hydroxyl groups) into all areas of the sample.

Analysis of the changes in intensity of the various six-fold-coordinated Sn sites after hydration (Figure 6, Figures S3 and S4 and Tables S1 and S2 in SI) suggests that the distribution has changed. For $x = 0.20$ to 0.40, the relative fraction attributed to the $Sn(OSn)_6$ environment decreases slightly on hydration (Figure 6f), compensated by a slight increase in the relative fraction of $Sn(OSn)_{6-z}(OY'_{Sn})_z$ ($z = 1$, 2, and 3) sites (Figure 6g). Since the new environments must originate from sites originally neighboring a vacancy, these findings suggest that the O vacancies do not reside in the Sn-rich regions of these samples. The total concentration of six-fold-coordinated Sn sites increases on hydration, and thus the relative intensity of the $Sn(OSn)_6$ site decreases, since few $Sn(OSn)_6$ sites are introduced by hydration. This is consistent with the theoretical results, which indicate that the vacancies preferentially locate between two Sn atoms and nnn to a Y cation. Hydration of such an environment will generally yield an increased concentration of six-fold-coordinated Sn sites with Y in their first coordination shells. In the case of $BaSn_{0.50}Y_{0.50}O_{2.75}$, we observe the presence of some $Sn(OSn)_{6-x}(OY'_{Sn})_x$ ($x > 0$) sites after hydration (Figure 5b) the fractional intensities of which are difficult to estimate by spectral deconvolution due to the poor signal-to-noise ratio. This suggests that there are some residual Sn−O−Sn defects in the dry material that can accommodate O vacancies, forming environments such as $Sn(OSn)_{5-x}(OY'_{Sn})_x(V_O^{\cdot\cdot}Sn)$, in keeping with the DFT finding that vacancies preferentially locate nnn to Y atoms. The presence of such defects is consistent with the lack of evidence for long-range cationic ordering in the XRD of this sample (these defects occurring in between more ordered Y/Sn domains, a topic further explored by the ^{17}O and ^{89}Y NMR experiments described below).

Table 2. Experimental (x = 0.1, 0.2, 0.3, 0.4, and 0.5) and Calculated (x = 0.074, 0.25, and 0.5) ^{119}Sn and ^{89}Y Isotropic Chemical Shifts for $Ba_{1-(x/2)}Sn_{1-(x/2)}Y_xO_3$ and $BaSn_{1-x}Y_xO_{3-(x/2)}$ Phases

site	C.N.[a]	environment[b]	exptl δ_{iso} (ppm)	calcd δ_{iso}[c] (ppm)		
				x = 0.074	x = 0.25	x = 0.5
^{119}Sn	6	$\mathbf{Sn}(OSn)_6$	−674 to −679[d]	−737[d] [41]	−629[d] [2]	—[e]
		$\mathbf{Sn}(OSn)_5(OY'_{Sn})$	−645	−695 [23]	—	—
		$\mathbf{Sn}(OSn)_4(OY'_{Sn})_2$	−618	−652 [1]	−587 [6]	—
		$\mathbf{Sn}(OSn)_3(OY'_{Sn})_3$	−595	—	—	—
		$\mathbf{Sn}(OSn)_2(OY'_{Sn})_4$	−579	—	−557 [1]	—
		$\mathbf{Sn}(OSn)_1(OY'_{Sn})_5$	−571	—	—	—
		$\mathbf{Sn}(OY'_{Sn})_6$	−564	—	—	−532 [4]
		$\mathbf{Sn}(OSn)_6Y^{\bullet}_{Ba}$	—	−730 [8]	−625 [4]	—
		$\mathbf{Sn}(OSn)_6(Y^{\bullet}_{Ba})_2$	—	—	—	−610 [2]
		$\mathbf{Sn}(OSn)_4(OY'_{Sn})_2Y^{\bullet}_{Ba}$	—	—	−601 [3]	—
		$\mathbf{Sn}(OSn)_4(OY'_{Sn})_2(Y^{\bullet}_{Ba})_2$	—	—	—	−588 [2]
		$\mathbf{Sn}(OSn)_2(OY'_{Sn})_4(Y^{\bullet}_{Ba})_2$	—	—	—	−563 [2]
		$\mathbf{Sn}(OSn)_1(OY'_{Sn})_5$	−571	—	—	—
		mean Sn six-fold coordinated		*−722 [73]*	*−603 [16]*	*−565 [10]*
	5	$\mathbf{Sn}(OSn)_5(V_O^{\bullet\bullet}Sn)$	−423	−537 [1]	—	—
		$\mathbf{Sn}(OSn)_2(OY'_{Sn})_3(V_O^{\bullet\bullet}Y'_{Sn})$		—	−407 [1]	—
		$\mathbf{Sn}(OSn)_4(OY'_{Sn})(V_O^{\bullet\bullet}Y'_{Sn})$		−502 [1]	—	—
		$\mathbf{Sn}(OSn)_3(OY'_{Sn})_2(V_O^{\bullet\bullet}Sn)$		−468 [1]	−433 [2]	—
		$\mathbf{Sn}(OY'_{Sn})_5(V_O^{\bullet\bullet}Y'_{Sn})$		—	—	−400 [4]
		mean Sn five-fold coordinated		*−502 [3]*	*−424 [3]*	*−400 [4]*
^{89}Y[f]	12	$Y^{\bullet}_{Ba}$	—	119 [1]	182 [1]	263 [2]
	6	Y'_{Sn}	300−343	77 [4]	167 [4]	303 [7]
	5	Y'_{Sn}	400−455	247 [1]	319 [1]	368 [2]
	4	Y'_{Sn}	—	—	—	473 [1]

[a] Coordination number. [b] The environment under consideration is highlighted in bold. [c] Theoretical shielding (σ) references in the form $\delta_{iso} = \sigma_{ref} + m_{ref}\sigma_{iso}$: ^{119}Sn [$\sigma_{ref}$ = 2123.0 ppm, m_{ref} = −0.8840, MAE = 55 ppm][13] and ^{89}Y [σ_{ref} = 2385.3 ppm, m_{ref} = −0.8945, MAE = 15 ppm][28] both derived by refit of previously published results. The numbers of environments of each type are given in square brackets as [N]; mean isotropic shifts over all equivalent environments are given for $N > 1$. [d] In undoped $BaSnO_3$, the experimental shift is −679 ppm while the calculated shifts are −736 and −771 ppm at the experimental and the optimized lattice constants, respectively. [e] Dash indicates environment not observed experimentally or theoretically. [f] $Y^{\bullet}_{Ba}$ coordination in optimized structures typically in the range 4−8 due to significant displacement of Y dopant.

^{119}Sn Shift Calculations. To explore the sensitivity of the ^{119}Sn shifts to local environment in more detail, we now compare the experimental results for the dry samples with those calculated using the GIPAW method (Table 2) for the configurations presented above (Table 1). A key finding from the calculations is that the calculated ^{119}Sn shift in the perovskite primitive cell of pure $BaSnO_3$ varies noticeably, depending on the structure used. The experimental and optimized lattice constants, a, of 4.116 and 4.180 Å yield values of −736 to −771 ppm, respectively, showing a significant gradient $d\delta_{iso}/da$ of −547 ppm/ Å, and suggesting a high degree of sensitivity of the NMR parameters to small structural variations. The computed ^{119}Sn shift of $BaSnO_3$ deviates by 92 ppm from the experimental value, exceeding the mean average error (MAE) of 55 ppm obtained when fitting the shielding reference, as described in the Computational Methods section. However, the gradient ($d\delta_{iso}/da$) derived above suggests that approximately 40% of this error can be attributed to the overestimation of the lattice constant in the calculation, despite the fact that this structural discrepancy is of a typical size for DFT geometry optimizations. Considering first the x = 0.074 configurations, the mean value of the chemical shift of the majority $Sn(OSn)_6$ environments is −737 ppm, while the $Sn(OSn)_5(OY'_{Sn})_1$ and $Sn(OSn)_4(OY'_{Sn})_2$ environments yield mean values of −695 and −652 ppm, respectively, corresponding to a shift per Y substituent of +42 and +43 ppm, respectively, in satisfactory agreement with the experimental trend (Table 2). The effect of nearest neighbor A-sublattice Y dopants on the chemical shift is much weaker, amounting to a variation of only +7 ppm per Y. The calculations also predict that the resonances associated with five-fold-coordinated Sn sites, while not experimentally resolved at this Y doping level, should lie approximately 180 to 200 ppm above the six-fold-coordinated peaks.

The mean calculated ^{119}Sn peak positions associated with six- and five-fold-coordinated Sn environments for the x = 0.25 compositions occur at −603 and −424 ppm (Table 2), in good agreement with approximate experimental midpoints (interpolated between x = 0.20 and 0.30) of −632 and −423 ppm (Table S1 in SI), respectively. The calculated change in the six-fold Sn shift due to nearest neighboring $Y^{\bullet}_{Ba}$ and Y'_{Sn} are approximately +4 and +18−21 ppm per Y, respectively, being significantly weaker than those calculated for x = 0.074, as observed experimentally for the resonances due to Sn environments with the most nearby Y cations but not for the environments with fewer nearby Y cations.

The assignment of the broad resonance observed experimentally at −564 ppm for x = 0.4 and 0.5 to the $Sn(OY'_{Sn})_6$ environment is supported by the corresponding mean calculated six-fold-coordinated Sn shift (averaging over all

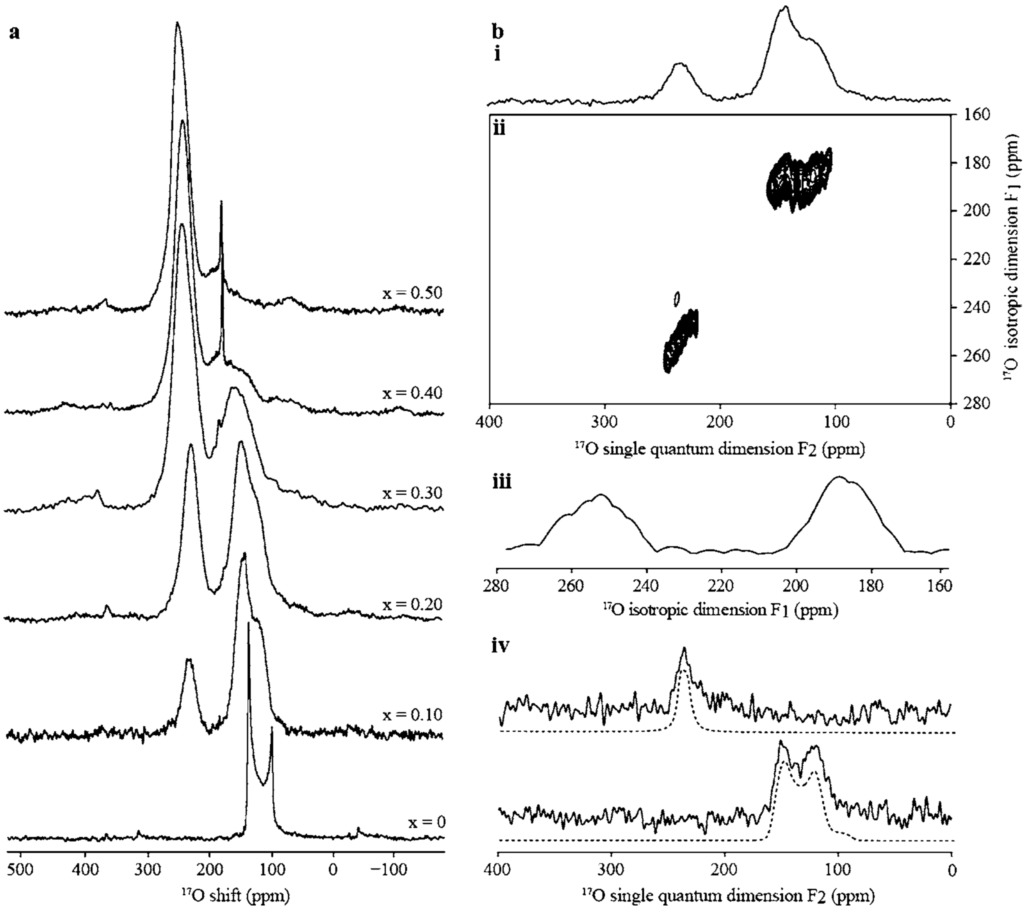

Figure 7. ^{17}O MAS NMR spectra of $BaSn_{1-x}Y_xO_{3-x/2}$. (a) Dry $BaSn_{1-x}Y_xO_{3-x/2}$, (b) Triple quantum MAS data of $BaSn_{0.90}Y_{0.10}O_{2.95}$. (i) Hahn echo spectrum. (ii) Two-dimensional (2D) triple-quantum MAS spectrum; 1320 transients were accumulated for each of the 16 t_1 increments. (iii) Isotropic projection of the 2D MQMAS spectra. (iv) Cross sections (full lines) extracted parallel to F_2 of the 2D MQMAS at δ_1 values of 254 (top) and 187 (bottom) ppm, along with best fit simulations (dashed lines).

relevant environments) of −565 ppm at $x = 0.5$ (Table 2). The mean shift of the majority $Sn(OY'_{Sn})_6$ environments, however, is approximately 33 ppm higher at −532 ppm. The effects of nearest neighbor $Y^{\bullet}_{Ba}$ and Y'_{Sn} dopants on the six-fold-coordinated Sn shift cannot be separately distinguished at this substitution level, but the trend in mean shifts obtained for $Sn(OSn)_6(OY'_{Sn})_0$, $Sn(OSn)_4(OY'_{Sn})_2$, $Sn(OSn)_2(OY'_{Sn})_4$, and $Sn(OSn)_0(OY'_{Sn})_6$ sites is very nearly linear with a gradient of +13 ppm per Y, regardless of the A-sublattice coordination of each site, suggesting that the contribution of the latter to the shift is negligible. The $x = 0.5$ results therefore confirm the trend toward a progressive weakening of the effects of both $Y^{\bullet}_{Ba}$ and Y'_{Sn} dopants upon neighboring Sn shifts as Y content increases. A calculated mean $Sn(OY'_{Sn})_5(V^{\bullet\bullet}_{O}Y'_{Sn})$ shift of −400 ppm is obtained for the five-coordinated Sn environments, consistent with the broad resonance observed at −423 ppm for substitution levels of $x \geq 0.20$.

^{17}O NMR. ^{17}O NMR spectra were acquired to provide further insight into the cation ordering. $BaSnO_3$ gives rise to a single resonance centered at 120 ppm with a distinctive second order quadrupolar line shape (Figure 7a; Figure S5 and Table S3 in SI; $\delta_{iso} = 152(1)$ ppm, $C_Q = 6.1(2)$ MHz, and $\eta_Q = 0.00(2)$). GIPAW calculations at the experimental lattice constant yield computed parameters $\delta_{iso} = 133$ ppm and $C_Q = 6.51$ MHz, and those in the optimized cell, $\delta_{iso} = 129$ ppm and $C_Q = 6.95$ MHz, all with $\eta_Q = 0.00$ consistent with the axial symmetry of O sites (Table 3). These are in reasonable agreement with the experimental values, although the difference in computed and experimental shifts exceeds the MAE of 12 ppm. Again, the computed gradients in NMR parameters across the range of lattice constants are significant, amounting to −74 ppm/Å and −6.84 MHz/Å for δ_{iso} and C_Q, respectively.

The introduction of Y dopants leads to the appearance of a second resonance centered at 236 ppm in the $BaSn_{0.90}Y_{0.10}O_{2.95}$ phase (Figures 7a and S6 in SI; central transition and full spectrum, respectively). The intensity of the resonance is proportional to the Y content and is therefore assigned to O in a $Sn-O-Y'_{Sn}$ linkage, Y substitution in the O local environment yielding a large change in isotropic chemical shift of more than +70 ppm. The additional sharp resonance at 186 ppm in $BaSn_{0.60}Y_{0.40}O_{2.80}$ and $BaSn_{0.50}Y_{0.50}O_{2.75}$ is tentatively assigned to O in water bound at the surfaces of the particles. Two-dimensional (2D) multiple-quantum MAS (MQMAS) experiments,[22,38,39] from which high resolution 1D spectra can be extracted, were performed for each sample to determine whether any other resonances are hidden under the $Y'_{Sn}-O-Sn$ and $Sn-O-Sn$ signals (Figure 7b and Figures S7−S11 in SI) and to extract the relevant ^{17}O NMR parameters (Table 3 and Table S3 in SI). The $Y'_{Sn}-O-Sn$ and $Sn-O-Sn$ environments are clearly resolved in all spectra, as shown in Figure 7b (ii) for $BaSn_{0.90}Y_{0.10}O_{2.95}$.

The calculated ^{17}O NMR parameters provide qualitative explanations for the broadening and shifts of the resonances on Y doping, identifying a wide range of chemical shifts that

Table 3. ^{17}O NMR Parameters Obtained for the Experimental $BaSn_{1-x}Y_xO_{3-(x/2)}$ (x = 0.1, 0.25, 0.5) Phases and Calculated $Ba_{1-(x/2)}Sn_{1-(x/2)}Y_xO_3$ and $BaSn_{1-x}Y_xO_{3-(x/2)}$ Structures (x = 0.074, 0.25, and 0.5)[a]

environment[b]	δ_{iso} (ppm)	C_Q (MHz)	η_Q	N[c]	δ_{iso} (ppm)	C_Q (MHz)	η_Q	N	δ_{iso} (ppm)	C_Q (MHz)	η_Q	N
					Experimental[d]							
	x = 0.1				x = 0.25[e]				x = 0.5			
Sn^{VI}–O–Sn^{VI}	168(5)	5.5(6)	0.0(0)	0.8(1)	176(17)	5.8(13)	0.3(3)	0.5(3)	202(6)	—[f]	—	0(1)
Sn^{VI}–O–$Y'^{\ VI}_{Sn}$	257(4)	3.8(3)	0.0(0)	0.2(1)	247(5)	3.7(7)	0.0(0)	0.5(3)	259(2)	3.4(6)	0.2(2)	1(1)
					Calculated							
	x = 0.074				x = 0.25				x = 0.5			
Sn^{VI}–O–Sn^{VI}	163	6.85	0.04	196	206	6.46	0.07	28	215	6.72	0.07	8
Sn^{VI}–O–Sn^{VI} ($Y^{\bullet}_{Ba}$)	173	5.53	0.44	4	231	5.24	0.49	6	249	4.80	0.55	4
Sn^{VI}–O–$Y'^{\ VI}_{Sn}$	235	3.92	0.06	21	253	3.93	0.13	18	268	2.83	0.17	22
Sn^{VI}–O–$Y'^{\ VI}_{Sn}$ ($Y^{\bullet}_{Ba}$)	—				—				268	3.56	0.35	8
Sn^{VI}–O_{ax}–$Y'^{\ V}_{Sn}$	284	3.38	0.08	1	—				—			
Sn^{V}–$O_{ax(2x)}$–$Y'^{\ V\,g}_{Sn}$	—				218	3.29	0.03	1	226	3.08	0.47	2
Sn^{V}–$O_{ax(2x)\text{-}eq}$–$Y'^{\ IV\,h}_{Sn}$	—				—				240	3.02	0.25	2
Sn^{VI}–O_{eq}–$Y'^{\ V}_{Sn}$	260	3.78	0.24	4	281	3.39	0.24	4	292	2.26	0.50	4
Sn^{V}–O_{eq}–$Y'^{\ VI}_{Sn}$	256	4.75	0.45	3	265	5.14	0.40	6	281	4.21	0.43	12
Sn^{V}–$O_{eq\ (2x)}$–$Y'^{\ V\,i}_{Sn}$	—				—				303	4.51	0.66	4
Sn^{VI}–$O_{eq\ (2x)}$–$Y'^{\ IV\,i}_{Sn}$	—				—				331	2.67	0.59	2
Sn^{VI}–O_{ax}–Sn^{V}	127	6.51	0.02	3	—				—			
Sn^{V}–$O_{ax(2x)}$–$Sn^{V\,g}$	—				118	6.02	0.02	1	—			
Sn^{VI}–O_{eq}–Sn^{V}	189	7.36	0.26	9	233	6.65	0.24	6	—			

[a] Theoretical shielding (σ) reference in form $\delta_{iso} = \sigma_{ref} + m_{ref}\sigma_{iso}$ is σ_{ref} = 223.70 ppm, m_{ref} = −0.8876, MAE = 12.1 ppm.[27] Mean NMR parameters are given for environments represented by numbers of sites N larger than 1. Calculated δ_{iso}, C_Q, and η_Q for undoped $BaSnO_3$ are 133 ppm, 6.51 MHz, and 0.00, respectively, for the experimental structure, and 119 ppm, 6.95 MHz, and 0.00 for the optimized structure. Experimental δ_{iso}, C_Q, and η_Q for undoped $BaSnO_3$ are 152(1) ppm, 6.1(2) MHz, and 0.0(2), respectively (Table S3). [b] The environments list the two closest cation species and their coordination numbers, the latter denoted by superscripts. Configurations neighboring $Y^{\bullet}_{Ba}$ dopants are also indicated. [c] Experimental: ratio of Sn^{VI}–O–Sn^{VI} site vs Sn^{VI}–O–$Y'^{\ VI}_{Sn}$ site. Calculated: number of sites represented by the environments. [d] The full experimental data are given in Table S3. [e] The experimental x = 0.25 NMR parameters values are obtained by averaging the x = 0.2 and 0.3 NMR parameters (Table S3). [f] Dash indicates environment not observed experimentally or theoretically. [g] Positioned axial to two O vacancies. [h] Positioned axial to two and equatorial to one O vacancy. [i] Positioned equatorial to two O vacancies.

depend both on the nature of the nearby cations, and, as in our earlier study of Mg-doped $LaGaO_3$[9] on the relative position of the vacancy. The calculated ^{17}O shifts at x = 0.074 are in reasonable agreement with experiment, confirming the experimentally observed large shift in the Sn^{VI}–O–Sn^{VI} isotropic shift due to nn Y^{VI} substitution, yielding a corresponding shift of +72 ppm (Table 3). A group of more numerous O environments associated predominantly with majority Sn^{VI}–O–Sn^{VI} sites (plus a much smaller number of Sn^{VI}–O_{ax}–Sn^{V}, i.e., sites where the vacancy is axial to the observed oxygen, O_{ax}) with mean δ_{iso} values of 162 ppm and large values of C_Q (6.8 MHz) [experimental: δ_{iso} = 168(2) ppm, C_Q = 5.5(6) MHz] is identified along with a smaller group associated predominantly with Sn^{VI}–O–$Y^{\ VI}_{Sn}$ (plus a smaller number of Sn^{VI}–O_{eq}–$Y'^{\ V}_{Sn}$, Sn^{V}–O_{eq}–$Y'^{\ VI}_{Sn}$ (i.e, equatorial to a vacancy) and Sn^{VI}–O_{ax}–$Y'^{\ V}_{Sn}$) sites with mean δ_{iso} values of 242 ppm, and a smaller C_Q value (3.97 MHz) [experimental: δ_{iso} = 247(4) ppm, C_Q = 3.4(4) MHz]. The calculations also suggest the presence of a third less numerous group of sites with mean parameters δ_{iso} = 184 ppm, C_Q = 6.80 MHz, and η_Q = 0.32 associated with Sn^{VI}–O_{eq}–Sn^{V} and a smaller number of Sn^{VI}–O–Sn^{VI} ($Y^{\bullet}_{Ba}$) sites. These sites are not observed experimentally as distinct resonances but may contribute to the observed distribution in chemical shifts.

The experimentally observed shift of the Sn–O–Sn environment gradually increases with progressive Y doping, the change being more sudden for the Sn–O–Y'_{Sn} environment where a 10 ppm shift is observed at $x \geq 0.3$ (i.e., with an onset at approximately the same stoichiometry at which the two-phase behavior attributed to Y/Sn clustering and ordering is observed in the ^{119}Sn NMR). Examining the x = 0.2 and 0.3 phases in more detail, two broad groups of ^{17}O resonances are observed, with fitted experimental parameters falling in the range δ_{iso} = 246–248(4) ppm and C_Q = 3.4–4.0(4) MHz for the higher frequency group assigned to Sn–O–Y'_{Sn} sites; and δ_{iso} = 170(5)–181(12) ppm and C_Q = 5.4(6)–6.1(10) MHz (Table S3) for the lower frequency group assigned to Sn–O–Sn. The calculations at x = 0.25 support the experimental values and assignment, providing mean NMR parameters δ_{iso} = 260 ppm, C_Q = 4.07 MHz, and η_Q = 0.20 (Table 3) for the high shift group comprising predominantly Sn^{VI}–O–$Y'^{\ VI}_{Sn}$ plus a smaller number of Sn^{VI}–O_{eq}–$Y'^{\ V}_{Sn}$ and Sn^{V}–O_{eq}–$Y'^{\ VI}_{Sn}$ sites; and δ_{iso} = 214 ppm, C_Q = 6.23 MHz, and η_Q = 0.16 for the low-shift group comprising a majority of Sn^{VI}–O–Sn^{VI}, Sn^{VI}–O_{eq}–Sn^{V}, Sn^{V}–$O_{ax(2x)}$–$Y'^{\ V}_{Sn}$ (the latter O site adopting a position axial to two vacancies), and Sn^{VI}–O–Sn^{VI} ($Y^{\bullet}_{Ba}$) sites. A single Sn^{V}–$O_{ax(2x)}$–Sn^{V} site arises at 118 ppm, but the relative scarcity of such sites means that they are unlikely to be resolved experimentally. Importantly, the calculations reproduce the experimentally observed general shift of the ^{17}O resonances with Y content, being most pronounced experimentally for the Sn–O–Sn environments.

Finally, the experimental spectra at the highest Y content x = 0.50 yields three groups of peaks: the first one assigned to Y'_{Sn}–O–Sn environments with fitted parameters δ_{iso} = 259(4) ppm and C_Q = 3.4(6) MHz (Tables 3 and S3); the second weaker

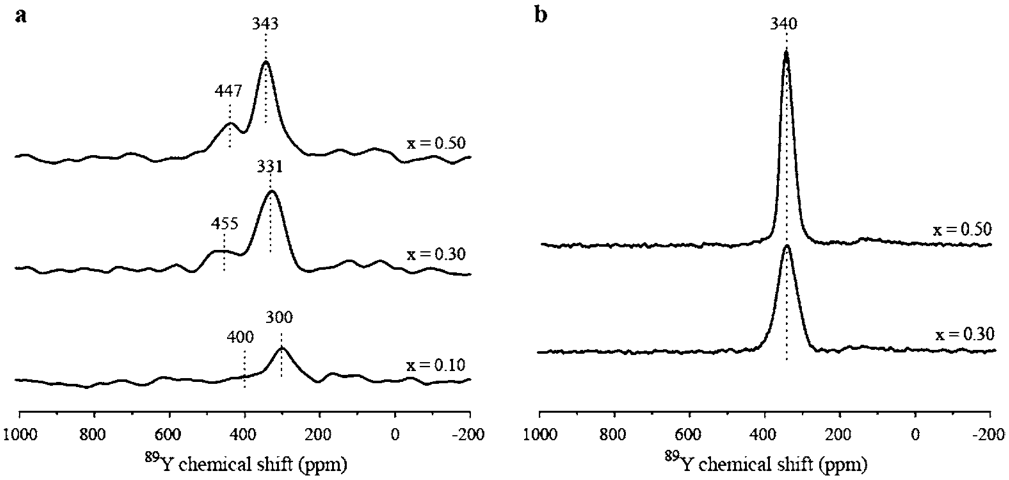

Figure 8. ^{89}Y MAS NMR spectra of $\mathrm{BaSn}_{1-x}\mathrm{Y}_x\mathrm{O}_{3-x/2}$: (a) dry materials acquired at 11.7 T and (b) hydrated materials acquired at 19.6 T. The resonances have been labeled with their isotropic chemical shifts.

resonance to Sn−O−Sn environments with $\delta_{\mathrm{iso}} = 202(6)$ ppm, $C_Q = 2.9(4)$ MHz, and $\eta_Q = 0.0(1)$ (Tables 3 and S3), and the third very weak resonance to surface water with $\delta_{\mathrm{iso}} = 186(1)$ ppm (Tables 3 and S3). The calculations provide no comparable NMR parameters for water and suggest instead the existence of a single broad group of resonances with shifts ranging from 215 to 312 ppm with mean NMR parameters $\delta_{\mathrm{iso}} = 266$ ppm, $C_Q = 3.81$ MHz, and $\eta_Q = 0.32$ (Table 3) comprising predominantly $\mathrm{Sn}^{\mathrm{VI}}{-}\mathrm{O}{-}\mathrm{Y}'^{\,\mathrm{VI}}_{\mathrm{Sn}}$, $\mathrm{Sn}^{\mathrm{VI}}{-}\mathrm{O}_{\mathrm{eq}}{-}\mathrm{Y}'^{\,\mathrm{V}}_{\mathrm{Sn}}$, $\mathrm{Sn}^{\mathrm{V}}{-}\mathrm{O}_{\mathrm{eq}}{-}\mathrm{Y}'^{\,\mathrm{VI}}_{\mathrm{Sn}}$, and $\mathrm{Sn}^{\mathrm{VI}}{-}\mathrm{O}{-}\mathrm{Sn}^{\mathrm{VI}}$ sites. The experimental shift of 202 ppm is not reproduced here, but the calculations do suggest that, if an observable number of $\mathrm{Sn}^{\mathrm{VI}}{-}\mathrm{O}{-}\mathrm{Sn}^{\mathrm{VI}}$ environments were to be present at $x = 0.50$, their mean shift would lie at 215 ppm, in good agreement with the assignment of the experimental 202 ppm group, albeit with a large C_Q of 6.72 MHz.

Considering the effects of Y clustering, the trends in the experimental ^{17}O shifts indicate that, if an observable number of $\mathrm{Y}'_{\mathrm{Sn}}{-}\mathrm{O}{-}\mathrm{Y}'_{\mathrm{Sn}}$ environments were present in any of the phases considered, then their experimental shifts would lie above 246 ppm. This is confirmed by the calculations. For example, the lowest-energy configuration found at $x = 0.074$ with a $\mathrm{Y}'_{\mathrm{Sn}}{-}\mathrm{O}{-}\mathrm{Y}'_{\mathrm{Sn}}$ environment yields a δ_{iso} value of 289 ppm. The absence of such resonances in the experimental spectra is in keeping with the strong nn $\mathrm{Y}'_{\mathrm{Sn}}$ repulsion discussed above. The energetics presented above do allow for the presence of $\mathrm{Y}'_{\mathrm{Sn}}{-}\mathrm{V}_{\mathrm{O}}^{\bullet\bullet}{-}\mathrm{Y}'_{\mathrm{Sn}}$ defect trimers, but these complexes would introduce only $\mathrm{Y}'^{\,\mathrm{V}}_{\mathrm{Sn}}{-}\mathrm{O}_{\mathrm{eq}}{-}\mathrm{Sn}^{\mathrm{VI}}$ and $\mathrm{Y}'^{\,\mathrm{V}}_{\mathrm{Sn}}{-}\mathrm{O}_{\mathrm{ax}}{-}\mathrm{Sn}^{\mathrm{VI}}$ environments into the O sublattice. The shifts due to such trimers, if present, will likely not be separately resolvable from the effects of more isolated Y dopants.

^{89}Y NMR. ^{89}Y NMR spectra were obtained for $\mathrm{BaSn}_{1-x}\mathrm{Y}_x\mathrm{O}_{3-x/2}$ at only three doping levels x = 0.1, 0.3, and 0.5 due to the long acquisition times required to perform ^{89}Y NMR, particularly in systems with very long ^{89}Y T_1 relaxation times and low Y contents. The main environment at 300 ppm in the dry compounds (Figure 8a, Table 2) is assigned to six-fold-coordinated $\mathrm{Y}'^{\,\mathrm{VI}}_{\mathrm{Sn}}$ environments in agreement with previously published results for other samples containing Y in the same coordination environment.[28,37,40−49] The resonance moves monotonically from 300 to 343 ppm with increasing Y content, a trend that is consistent with all the probe nuclei investigated here. Given the finding from ^{17}O NMR, that the first B-sublattice cation coordination shell is fully occupied by Sn atoms, the shift must be sensitive to the increasing number of Y cations in the second B-sublattice cation coordination shell, presumably altering the Y−O bond lengths and bond angles of the probed species (Y). In the case of $\mathrm{BaSn}_{0.90}\mathrm{Y}_{0.10}\mathrm{O}_{2.95}$ the second cation coordination shell is predominantly occupied by Sn cations, while for $\mathrm{BaSn}_{0.70}\mathrm{Y}_{0.30}\mathrm{O}_{2.85}$ it is occupied by both Sn and Y cations, consistent with the broader line shape of the six-coordinated Y environments observed in the latter phase. The sharper line shape observed for $\mathrm{BaSn}_{0.50}\mathrm{Y}_{0.50}\mathrm{O}_{2.75}$ provides further support for the presence of a high degree of Y/Sn ordering in the structure, suggesting the presence of a more limited range of possible Y and Sn arrangements in the second B-sublattice cation coordination shell of each $\mathrm{Y}'_{\mathrm{Sn}}(\mathrm{OSn})_6$ site. Only $\mathrm{Y}'_{\mathrm{Sn}}$ sites would be expected in this shell in the case of ideal alternating Y/Sn order.

A second resonance is clearly observed for $\mathrm{BaSn}_{0.70}\mathrm{Y}_{0.30}\mathrm{O}_{2.85}$ and $\mathrm{BaSn}_{0.50}\mathrm{Y}_{0.50}\mathrm{O}_{2.75}$ at higher frequencies of 455−447 ppm. The $\mathrm{BaSn}_{0.90}\mathrm{Y}_{0.10}\mathrm{O}_{2.95}$ phase gives rise to a weaker resonance at 400 ppm, observed more clearly in the deconvoluted spectrum (Figure S13a, SI). To assist in the assignment of this resonance, the ^{89}Y chemical shifts observed for a variety of different Y local environments in a range of materials are plotted as a function of Y coordination number in Figure 9. While the shift ranges observed for different coordination numbers overlap, there is a clear overall trend toward an increase in shift with decreasing coordination number, suggesting that the second resonance in the present phases arises from a lower coordinated Y site. We can therefore confidently assign the resonance at 447−455 ppm to a five-fold-coordinated $\mathrm{Y}'^{\,\mathrm{V}}_{\mathrm{Sn}}$ environment. To the best of our knowledge, this is the first reported spectrum of a five-fold-coordinated Y cation. The $\mathrm{Y}'^{\,\mathrm{V}}_{\mathrm{Sn}}$ resonances disappear upon hydration (Figure 8b) as the O vacancies are progressively occupied by OH groups, providing a convincing confirmation of the assignments.

The computed mean Y shifts at $x = 0.074$ differ significantly from the experimental values, being 77, 247, and 119 ppm for six- and five-fold-coordinated $\mathrm{Y}'_{\mathrm{Sn}}$ and $\mathrm{Y}^{\bullet}_{\mathrm{Ba}}$ environments, respectively (Table 2), increasing to 167, 319, and 182 ppm, respectively, at $x = 0.25$, and further to 303, 368, and 263 ppm, respectively, at $x = 0.5$. Interestingly, the next highest energy Y/Sn ‘ordered’ state at $x = 0.5$ lies at only 9 kJ/mol above the

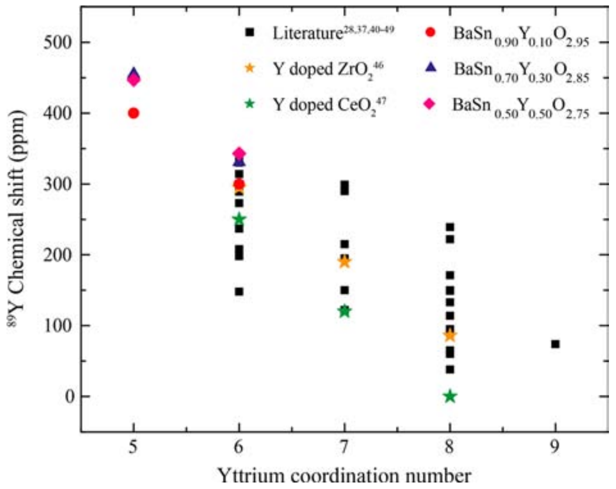

Figure 9. Comparison of the experimental shifts for five- and six-coordinated Y environments in $BaSn_{1-x}Y_xO_{3-x/2}$, $x = 0.10$ (red circle), 0.30 (blue triangle), and 0.50 (purple star), and the ^{89}Y chemical shifts reported for stoichiometric materials in the literature (black squares).[28,37,40−49] The shifts for the different Y coordination environments in Y-doped ZrO_2[46] and CeO_2[47] are shown as orange and green stars, respectively.

ground state, and contains a four-fold-coordinated $Y_{Sn}'^{\,IV}$ environment with a shift of 473 ppm, confirming the progressive increase in Y shift with decreasing coordination number. The $x = 0.5$ $Y_{Sn}'^{\,VI}$ shift is in satisfactory agreement with experiment (303 ppm vs 343 ppm), but the $Y_{Sn}'^{\,V}$ shift and the differences in five- and six-fold-coordinated shifts are both significantly underestimated, the deviations from experiment growing progressively larger as Y content falls. The errors evident across the doping range are likely meaningful, given that the previous MAE in Y shifts computed across a broad range of compounds (including the $Y_2Sn_2O_7$ pyrochlore) amounts to only 15 ppm.[28] Further investigations of the accuracy of Y dopant shifts in the closely related $BaZrO_3$ perovskite are underway. The argument presented above for Sn sites that electronic structure effects supersede lattice dilation in determining the variations in shift with dopant concentration apparently also applies to Y shifts (see SI for further discussion).

The experimental ratios of the weights of $Y_{Sn}'^{\,V}$ to $Y_{Sn}'^{\,VI}$ sites at the three doping levels considered were extracted by spectral deconvolution (Figure S13 in SI) and are compared to the similarly obtained Sn^{V} to Sn^{VI} ratios in Table 4. For $BaSn_{0.90}Y_{0.10}O_{2.95}$ and $BaSn_{0.70}Y_{0.30}O_{2.85}$ the ratios of five- to six-fold-coordinated environments are very similar for both Sn and Y, indicating that O vacancies order randomly at low doping levels. In $BaSn_{0.50}Y_{0.50}O_{2.75}$, meanwhile, the five- to six-fold-coordinated ratio is 0.34 to 0.66, being significantly smaller than the ratio 0.44 to 0.56 obtained for Sn sites. These ratios should be equal in the case of perfect Y/Sn ordering. The discrepancy can be ascribed to a number of factors, as follows. First, ^{89}Y relaxation times are extremely long, and while spectra acquired with both longer and shorter recycle delays than the delay (250 s) used to acquire the spectra shown here do not show resonances with noticeably different relative intensities, it is difficult to completely exclude the possibility that the relaxation time for the $Y_{Sn}'^{\,V}$ environment is longer than that of the $Y_{Sn}'^{\,VI}$ environment, leading to a reduction in the intensity of the former sites relative to the latter. Second, it is possible that a small fraction of the doped Y atoms enter the lattice as $Y_{Ba}^{\bullet}$ rather than Y_{Sn}' sites, a substitution that calculations have suggested becomes more favorable at higher Y contents. Such substitution gives rise to stoichiometries $(Ba_{1-2b}Y_{2b})(Sn_{0.5+b}Y_{0.5-b})O_{2.75+1.5b}$, where the presence of $Y_{Ba}^{\bullet}$ dopants reduces the O vacancy content and therefore the ratio of five- to six-fold-coordinated sites for both Y and Sn. Sn−O−Sn environments are also created, consistent with the ^{17}O NMR. Higher-fold-coordinated $Y_{Ba}^{\bullet}$ sites should, in principle, be visible in the ^{89}Y NMR spectrum at frequencies below the six-fold-coordinated Y resonance, according to the trends shown in Figure 9. However, the DFT optimizations discussed above show that the actual coordination experienced by $Y_{Ba}^{\bullet}$ dopants lies in the range from 4 to 8 (with four short and four longer Y−O bonds, Figure S1a, or with six short and six longer Y−O bonds, Figure S1b), as a consequence of the displacement of Y cations off the AO_{12} cube centers. This distortion of the AO_{12} site to form a lower coordinated environment will likely result in a shift closer to that of the six-fold $Y_{Sn}'^{\,VI}$ site. This, combined with the likelihood that such environments may be quite disordered, given that many different Y/Sn arrangements will be present on the neighboring B-sublattice sites, may result in broad, weak signals that will be difficult to resolve.

Table 4. Experimental Intensity Ratios for Five- and Six-Fold-Coordinated Y and Sn Environments Extracted from Deconvolution of the ^{89}Y and ^{119}Sn NMR Spectra, respectively, of $BaSn_{1-x}Y_xO_{3-x/2}$ Phases

	^{89}Y NMR		^{119}Sn NMR	
x	$Y_{Sn}'^{\,V}$	$Y_{Sn}'^{\,VI}$	Sn^{V}	Sn^{VI}
0.10	0.08(2)	0.92(2)	0.00(4)	1.00(4)
0.30	0.22(2)	0.78(2)	0.21(3)	0.79(3)
0.50	0.34(2)	0.66(2)	0.44(1)	0.56(1)

^{119}Sn MAS NMR at High Temperature. Although little discussed in the literature, hydration of the material requires a sufficiently high mobility of O vacancies that they can move to the particle surface to react with water molecules. For this reason, hydration of the present and related phases is generally performed at high temperatures between 200 and 800 °C, leading to a trade-off between incorporation and desorption of water. In order to investigate O vacancy transport in the present material, we have recorded the high temperature ^{119}Sn MAS NMR spectra for $BaSn_{0.50}Y_{0.50}O_{2.75}$ (Figure 10). At room temperature, the five- and six-fold-coordinated Sn environments are clearly resolved at approximately −420 and −565 ppm, respectively. As the temperature increases, a broad component appears at 400 °C positioned between these two environments at approximately −497 ppm. Upon additional heating, the intensity of the new resonance increases, and its line width narrows. While the narrowing of the original resonances from room temperature to 200 °C and above is ascribed to an increase in ν_r from 4 to 6 kHz, the narrowing observed for the new resonance is ascribed to an increase in ionic motion. This new resonance is ascribed to a Sn cation with an average coordination number of 5.5 on the NMR time scale, resulting from O ion hopping from a SnO_6 octahedron into a vacant anion site neighboring an initially five-fold-coordinated cation, leading to a swapping of Sn coordination environments (Figure 1b). This process starts above 200 °C, the coalescence requiring a jump frequency k greater than the

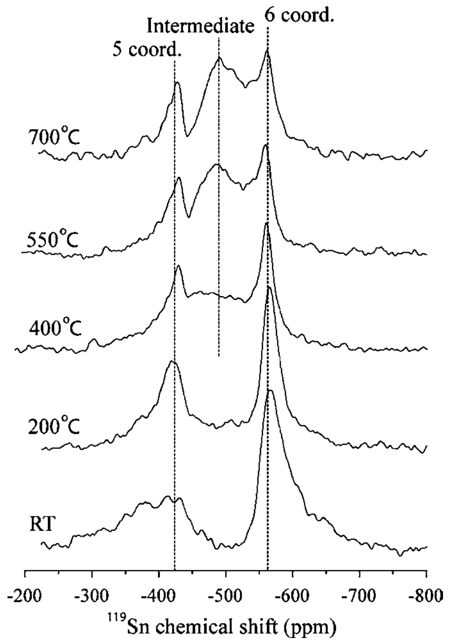

Figure 10. High-temperature ^{119}Sn MAS NMR spectra of the dry $BaSn_{0.50}Y_{0.50}O_{2.75}$ sample. The RT and 200 °C data were obtained at MAS rate of ν_r = 4 kHz, while above 200 °C, ν_r was set to 6 kHz.

frequency separation $\Delta\nu$ between the two resonances and given by[50]

$$k = \frac{\pi \Delta \nu}{\sqrt{2}} \tag{5}$$

which yields approximately k = 58 kHz. This onset of such motion is consistent with the previously reported hydration behavior, where significant water uptake starts at around 300 °C,[1] this also being the temperature at which loss of structural water is seen in the TGA experiments. The spectra do not show the simple coalescence behavior expected for two-site exchange with a single correlation time, residual resonances at −423 and −564 ppm persisting at the highest temperatures. A similar phenomenon has been reported previously by Wang et al.[51] for fluoride ions in α-PbF_2 and is ascribed to a distribution of motional correlation times. This distribution will result in the apparent coalescence of the resonances from the subset of spins with short correlation times, the residual spins appearing to be in the "slow" motional regime (i.e. with correlation times longer than 0.2 ms). The fraction of spins in the slow motional regime decreases as the temperature is increased, with few if any spins in the intermediate regime being detected at any temperature. The distribution of correlation times is likely a consequence of the incomplete ordering of the cation sublattice combined with disorder in the anion/vacancy sublattice. Studies are also underway to investigate the role that water plays in altering the activation energy of the O ion migration, a phenomenon that has been explored by simulations and that may also contribute to the distribution of correlation times.[52,53]

■ CONCLUSION

In summary, the present detailed experimental NMR and theoretical study provides strong evidence for random Y distributions at low doping levels, and short-range Y'_{Sn}−O−Sn ordering at high substitution levels in $BaSn_{1-x}Y_xO_{3-x/2}$. The tendency for Y and Sn to alternate on the B site of the perovskite structure was observed by ^{119}Sn NMR in $BaSn_{0.5}Y_{0.5}O_{2.75}$, with all the Sn environments being surrounded by close to six Y cations in the first B-site cation coordination shell in $BaSn_{0.50}Y_{0.50}O_{2.75}$. This ordering is in agreement with the ^{17}O NMR spectra, which for $BaSn_{0.50}Y_{0.50}O_{2.75}$ is dominated by a Y'_{Sn}−O−Sn resonance. No Y'_{Sn}−O−Y'_{Sn} local environments were observed; this cannot be explained by the preferential location of the vacancies between Y cations, as no preference for five-coordinate over six-coordinate Y environments was seen by ^{89}Y NMR. Indeed, the intensity ratio of the five- to six-coordinate environments in $BaSn_{0.50}Y_{0.50}O_{2.75}$ is actually higher in the ^{119}Sn NMR spectrum than in the ^{89}Y NMR spectrum.

Even $BaSn_{0.50}Y_{0.50}O_{2.75}$ contains residual Sn−O−Sn environments, consistent with the lack of long-range cation ordering observed in our study, as probed by XRD. This is ascribed to incomplete Y substitution, and/or the presence of some Y^{3+} cations on the A site ($Y^{\bullet}_{Ba}$) as has been reported for Y substituted $BaZrO_3$.[17] A-site substitution of Y is driven by or is coupled to BaO loss during sintering and leads to the stoichiometry $Ba_{1-2b}Y_{2b}(Sn_{0.5+b}Y_{0.5-b})O_{2.75+1.5b}$ and the formation of Sn−O−Sn groups. Preferential location of the O vacancies in between two Sn atoms, could account for the different five- to six-coordinate ratios for Sn and Y. However, no clear ^{89}Y signature for $Y^{\bullet}_{Ba}$ substitution was observed experimentally, most likely due to the inherent low sensitivity of this nucleus. Furthermore, the DFT calculations indicate that a $Y^{\bullet}_{Ba}$ site if present will be severely distorted yielding a chemical shift approaching that of a Y'^{VI}_{Sn} site. Long-range cation ordering is presumably difficult to achieve during synthesis due to the low diffusivities of the cations, and the relatively weak driving force for ordering revealed by the calculations.

Finally, these results have significant implications for proton conductivity given that they indicate that the majority of the protons in the hydrated material will coordinate with the same type of oxygen linkage (Y'_{Sn}−O−Sn) for locally ordered $BaSn_{0.50}Y_{0.50}O_{2.75}$ (the residual protons being linked to Sn−O−Sn groups). The ability of the structure to accommodate Y'_{Sn}−O−Sn ordering allows very high levels of Y and thus vacancies (and protons on hydration) to be incorporated into the structure without forming basic O sites such as Y'_{Sn}−O−Y'_{Sn} environments. The high concentration of Y'_{Sn}−O−Sn and lack of Y'_{Sn} −O−Y'_{Sn} environments allow hops to occur between similar local environments, without trapping on the more basic Y'_{Sn}−O−Y'_{Sn} environments. Such cation ordering has not been seen in the Y-substituted $BaZrO_3$ and $BaCeO_3$ systems, which show higher conductivity at lower Y substitution levels.[1] Thus, we believe that the high conductivity of $BaSn_{0.50}Y_{0.50}O_{2.75}$ is due to the predominance of a single O site and the lack of basic Y'_{Sn}−O−Y'_{Sn} sites, combined with the large number of protons in the material due to the high substitution level. Finally, the O conduction required for hydration of such a protonic conductor was observed via the exchange of five- and six-coordinated Sn environments in $BaSn_{0.50}Y_{0.50}O_{2.75}$ at 400 °C and above.

■ ASSOCIATED CONTENT

Ⓢ Supporting Information

Additional discussion of the ^{119}Sn and ^{17}O data, shielding and EFG tensor conventions, optimized calculated geometries of $Y^{\bullet}_{Ba}$ (Figure S1), ^{119}Sn spectra of all materials (Figure S2), spectral deconvolution of the ^{119}Sn spectra of the dry (Figure S3) and hydrated (Figure S4) materials, fit of the ^{17}O spectra of $BaSnO_3$ (Figure S5), full spectral width 1D ^{17}O spectra of $BaSn_{1-x}Y_xO_{3-x/2}$ (Figure S6), ^{17}O MQMAS spectra of

$BaSn_{1-x}Y_xO_{3-x/2}$ (Figures S7–S11), ^{17}O spectrum of $BaSn_{0.60}Y_{0.40}O_{2.80}$ (Figure S12) at 21.1 T, spectral deconvolution of the ^{89}Y spectra of $BaSn_{1-x}Y_xO_{3-x/2}$ (x = 0.10, 0.30, and 0.50) (Figure S13), ratios and isotropic chemical shifts of the different six-coordinate Sn from ^{119}Sn spectra of the dry (Table S1) and hydrated materials (Table S2), ^{17}O NMR parameters obtained from the MQMAS data (Table 3), details of all configurations considered in DFT calculations and corresponding optimized structures and GIPAW NMR parameters. This material is available free of charge via the Internet at http://pubs.acs.org.

AUTHOR INFORMATION

Corresponding Author

cpg27@cam.ac.uk

Notes

The authors declare no competing financial interest.

ACKNOWLEDGMENTS

L.B., F.B., and C.P.G thank the NSF via Grant DMR0804737 and NYSTAR for support. F.B. also thanks the French foreign office for a post doctoral Lavoisier fellowship 2007–2008 (Grant 530227G) and the EU Marie Curie actions FP7 for an International Incoming fellowship (Grant 275212). We thank Dr. Martine Ziliox (Center for Structural Biology, State University of New York, Stony Brook, NY) and Dr. Boris Itin (New York Structural Biology Center, New York City, NY) for technical assistance with the NMR measurements at 14.1 and 21.1 T, respectively. We also thank Dr. Ian Farnan (Department of Earth Sciences, University of Cambridge, UK) for access to the 7.5 mm HX Chemagnetics probe and the 500 MHz Varian spectrometer. Part of this work is sponsored by the National High Magnetic Field Laboratory through National Science Foundation Cooperative Agreement DMR0654118 and by the State of Florida; we thank both Drs. Zhehong Gan and Ivan Hung for their help with the work performed at 830 MHz in this facility. The UK 850 MHz solid-state NMR Facility was also used in this research; funds came from EPSRC and BBSRC, as well as the University of Warwick including partial funding through Birmingham Science City Advanced Materials Projects 1 and 2 supported by Advantage West Midlands (AWM) and the European Regional Development Fund (ERDF). Also acknowledged is an allocation of time upon the NANO computer cluster at the Centre for Functional Nanomaterials, Brookhaven National Laboratory, United States, which is supported by the U.S. Department of Energy, Office of Basic Energy Sciences, under Contract DE-AC02-98CH10886. C.P.G.'s and D.S.M.'s membership of the UK's HPC Materials Chemistry Consortium is gratefully acknowledged, as funded by the EPSRC (EP/F067496). This work made use of the facilities of HECToR, the UK's national high-performance computing service, which is provided by UoE HPCx Ltd at the University of Edinburgh, Cray Inc., and NAG Ltd., and funded by the Office of Science and Technology through EPSRC's High End Computing Programme.

REFERENCES

(1) Kreuer, K. D. *Ann. Rev. Mater. Res.* **2003**, *33*, 333.
(2) Murugaraj, P.; Kreuer, K. D.; He, T.; Schober, T.; Maier, J. *Solid State Ionics* **1997**, *98*, 1.
(3) Náray-Szabó, St. V. *Naturwissenschaften* **1943**, *31*, 202.
(4) Paulose, K. V.; Murugaraj, P.; Koshy, J.; Damodaran, A. D. *Jpn. J. Appl. Phys.* **1992**, *31*, 1323.
(5) Koshy, J.; Kumar, K. S.; Kurian, J.; Yadava, Y. P.; Damodaran, A. D. *Bull. Mater. Sci.* **1994**, *17*, 577.
(6) Megaw, H. D. *Proc. Phys. Soc* **1946**, *58*, 133.
(7) Pickard, C. J.; Mauri, F. *Phys. Rev. B* **2001**, *63*, 245101.
(8) Yates, J. R.; Pickard, C. J.; Mauri, F. *Phys. Rev. B* **2007**, *76*, 024401.
(9) Blanc, F.; Middlemiss, D. S.; Gan, Z.; Grey, C. P. *J. Am. Chem. Soc.* **2011**, *133*, 17662.
(10) Ishihara, T.; Matsuda, H.; Takita, Y. *J. Am. Chem. Soc.* **1994**, *116*, 3801.
(11) Feng, M.; Goodenough, J. B. *Eur. J. Solid State Inorg. Chem.* **1994**, *31*, 663.
(12) Clayden, N. J.; Dobson, C. M.; Fern, A. *J. Chem. Soc., Dalton Trans.* **1989**, 843.
(13) Mitchell, M. R.; Reader, S. W.; Johnston, K. E.; Pickard, C. J.; Whittle, K. R.; Ashbrook, S. E. *Phys. Chem. Chem. Phys.* **2011**, *13*, 488.
(14) Ashbrook, S. E.; Smith, M. E. *Chem. Soc. Rev.* **2006**, *35*, 718.
(15) Bastow, T. J.; Dirken, P. J.; Smith, M. E.; Whitfield, H. J. *J. Phys. Chem.* **1996**, *100*, 18539.
(16) Kroger, F. A.; Vink, H. J. In *Solid State Physics: Advances in Research and Applications*; Seitz, F.; Turnbull, D., Eds.; Academic: New York, 1956; Vol. 3, p 307.
(17) Yamazaki, Y.; Hernandez-Sanchez, R.; Haile, S. M. *J. Mater. Chem.* **2010**, *20*, 8158.
(18) Babilo, P.; Haile, S. M. *J. Am. Ceram. Soc.* **2005**, *88*, 2362.
(19) Bielecki, A.; Burum, D. P. *J. Magn. Reson., Ser. A* **1995**, *116*, 215.
(20) Grutzner, J. B.; Stewart, K. W.; Wasylishen, R. E.; Lumsden, M. D.; Dybowski, C.; Beckmann, P. A. *J. Am. Chem. Soc.* **2001**, *123*, 7094.
(21) Van Moorsel, G.-J. M. P.; Van Eck, E. R. H.; Grey, C. P. *J. Magn. Reson., Ser. A* **1995**, *113*, 159.
(22) Amoureux, J. P.; Fernandez, C.; Steuernagel, S. *J. Magn. Reson., Ser. A* **1996**, *123*, 116.
(23) Bastow, T. J.; Stuart, S. N. *Chem. Phys.* **1990**, *143*, 459.
(24) van Beek, J. D. *J. Magn. Reson.* **2007**, *187*, 19.
(25) Bak, M.; Rasmussen, J. T.; Nielsen, N. C. *J. Magn. Reson.* **2000**, *147*, 296.
(26) Hodgkinson, P.; Emsley, L. *Prog. Nucl. Magn. Reson. Spectrosc.* **2000**, *36*, 201.
(27) Middlemiss, D. S.; Blanc, F.; Pickard, C. J.; Grey, C. P. *J. Magn. Reson.* **2010**, *204*, 1.
(28) Reader, S. W.; Mitchell, M. R.; Johnston, K. E.; Pickard, C. J.; Whittle, K. R.; Ashbrook, S. E. *J. Phys. Chem. C* **2009**, *113*, 18874.
(29) Clark, S. J.; Segall, M. D.; Pickard, C. J.; Hasnip, P. J.; Probert, M. J.; Refson, K.; Payne, M. C. *Z. Kristallogr.* **2005**, *220*, 567.
(30) Profeta, M.; Mauri, F.; Pickard, C. J. *J. Am. Chem. Soc.* **2003**, *125*, 541.
(31) Perdew, J. P.; Burke, K.; Ernzerhof, M. *Phys. Rev. Lett.* **1996**, *77*, 3865.
(32) Bevillon, E.; Dezanneau, G.; Geneste, G. *Phys. Rev. B* **2011**, *83*, 174101.
(33) Wang, Y. Z.; Bevillon, E.; Chesnaud, A.; Geneste, G.; Dezanneau, G. *J. Phys. Chem. C* **2009**, *113*, 20486.
(34) Bevillon, E.; Geneste, G. *Phys. Rev. B* **2008**, *77*, 143113.
(35) Bjorketun, M. E.; Sundell, P. G.; Wahnstrom, G. *Faraday Discuss.* **2007**, *134*, 247.
(36) Subramanian, M. A. *J. Solid State Chem.* **1994**, *111*, 134.
(37) MacKenzie, K. J. D.; Smith, M. E. *Multinuclear Solid-State NMR of Inorganic Materials*; Pergamon Press: Oxford, 2002.
(38) Frydman, L.; Harwood, J. S. *J. Am. Chem. Soc.* **1995**, *117*, 5367.
(39) Medek, A.; Harwood, J. S.; Frydman, L. *J. Am. Chem. Soc.* **1995**, *117*, 12779.
(40) Ashbrook, S. E.; Whittle, K. R.; Lumpkin, G. R.; Farnan, I. *J. Phys. Chem. B* **2006**, *110*, 10358.
(41) Dupree, R.; Smith, M. E. *Chem. Phys. Lett.* **1988**, *148*, 41.
(42) Becerro, A. I.; Escudero, A.; Florian, P.; Massiot, D.; Alba, M. D. *J. Solid State Chem.* **2004**, *177*, 2783.
(43) Harazono, T.; Watanabe, T. *Bull. Chem. Soc. Jpn.* **1997**, *70*, 2383.
(44) Grey, C. P.; Smith, M. E.; Cheetham, A. K.; Dobson, C. M.; Dupree, R. *J. Am. Chem. Soc.* **1990**, *112*, 4670.

(45) Florian, P.; Massiot, D.; Humbert, G.; Coutures, J. P. *C. R. Acad. Sci., Ser. IIb Mec., Phys., Chim., Astron.* **1995**, *320*, 99.

(46) Kawata, K.; Maekawa, H.; Nemoto, T.; Yamamura, T. *Solid State Ionics* **2006**, *177*, 1687.

(47) Jain, P.; Avila-Paredes, H. J.; Gapuz, C.; Sen, S.; Kim, S. *J. Phys. Chem. C* **2009**, *113*, 6553.

(48) Kim, N.; Stebbins, J. F. *Chem. Mater.* **2007**, *19*, 5742.

(49) Harvey, E. J.; Ashbrook, S. E.; Lumpkin, G. R.; Redfern, S. A. T. *J. Mater. Chem.* **2006**, *16*, 4665.

(50) Levitt, M. H. *Spin Dynamics*; Wiley: Chichester, 2000.

(51) Wang, F.; Grey, C. P. *J. Am. Chem. Soc.* **1998**, *120*, 970.

(52) Islam, M. S. *J. Mater. Chem* **2000**, *10*, 1027.

(53) Islam, M. S.; Slater, P. R.; Tolchard, J. R.; Dinges, T. *Dalton Trans.* **2004**, 3061.